International Journal of Heat and Mass Transfer 209 (2023) 124103

Contents lists available at ScienceDirect

International Journal of Heat and Mass Transfer

journal homepage: www.elsevier.com/locate/hmt

Bubble growth on a smooth metallic surface at atmospheric and sub-atmospheric pressure

M.M. Mahmoud [a], T.G. Karayiannis [b,*]

[a] Faculty of Engineering, Zagazig University, Zagazig 44519, Egypt
[b] Department of Mechanical and Aerospace Engineering, Brunel University London, Uxbridge UB8 3PH, UK

ARTICLE INFO

Article history:
Received 10 July 2022
Revised 8 November 2022
Accepted 15 March 2023
Available online 28 March 2023

Keywords:
Pool boiling
Bubble growth
Bubble growth mechanism
Copper surface

ABSTRACT

Bubble growth rate is one of the most important parameters required for the development of accurate mechanistic nucleate boiling heat transfer models. It is also very important for understanding the hydrodynamic forces and the mechanism of bubble departure. This paper presents an experimental study on bubble growth measurements in saturated pool boiling of deionized water on a plain copper surface at atmospheric and sub-atmospheric pressure. The measurements were conducted using a high-speed, high-resolution camera with a microscopic lens. The mechanisms of bubble growth are discussed, while the microlayer evaporation mechanism has been evaluated and discussed using the measured bubble growth curve. The estimated contribution of microlayer evaporation to a single bubble growth is about 70 %, while the contribution of latent heat transfer (evaporation) to the total heat transfer rate from the surface is about 30 %. The remaining 70 % is due to other mechanisms, i.e. conduction and convection. These values were obtained based on the analysis of the bubble growth curve only and agreed with some researchers who conducted local heat transfer measurements using integrated sensors or infrared thermography. These detailed measurement techniques cannot be used with the thick copper block tested in the current study, which was also tested by many researchers in literature and is representative of industrially used surfaces. It was also found that the bubble departure mechanism at atmospheric pressure is due to a static balance between surface tension and buoyancy forces while at sub-atmospheric pressure, it was between buoyancy and liquid inertia forces. The pressure did not have a significant effect on the characteristics of the dynamic contact angle, which was also measured from the instantaneous images of the bubble. It was concluded also that the force balance required for the accurate prediction of departure diameter should be conducted when the two forces are equal, which occurred at time less than the departure time and dynamic contact angle of about 45. In most bubble departure models, researchers recommended the balance to be conducted at the moment of departure when the bubble forms a neck with contact angle of 90^0 (underestimation to the surface tension force). The analysis of one of the commonly used homogeneous growth models indicated that for homogeneous bubble growth models to be applicable in nucleate boiling, an allowance must be made for the fact that the degree of superheat varies with time during a bubble growth period.

1. Introduction

There is a big challenge in cooling electronic equipment and high heat flux systems. Boiling is one of the most efficient methods recommended by researchers for electronics cooling. The tested fluids were either dielectric liquids (refrigerants) or water. Although refrigerants can achieve very low surface temperature, the maximum quantity of heat that can be dissipated from electronic equipment is very low compared to water. This is due to the poor thermophysical properties of refrigerants compared to water. Additionally, most refrigerants operate at high system pressure, which may add some complexity to the cooling system. On the contrary, water at atmospheric pressure can dissipate high heat fluxes compared to refrigerants but the surface temperature may exceed the allowable operating temperature in most electronics (85 °C in computer chips and 125 °C in Insulated Gate Bipolar Transistors, IGBTs). Boiling water at subatmospheric pressure may be a viable option to reduce the surface temperature in electronics below the allowable limit, i.e. in a closed loop such as a heat pipe or a ther-

* Corresponding author.
E-mail address: tassos.karayiannis@brunel.ac.uk (T.G. Karayiannis).

https://doi.org/10.1016/j.ijheatmasstransfer.2023.124103

Nomenclature

A_{int}	interfacial area, [m^2]
a	empirical exponent in Eq. (1)
b	empirical exponent in Eq. (1)
b^*	empirical constant in Eq. (25)
C	constant in Eq. (1) or curvature factor in Eq. (3)
C_1	empirical growth constant in Cooper model
C_2	constant in initial thickness in Cooper model
c_{pl}	liquid specific heat, [J/kg K]
D_d	bubble departure diameter, [m]
D_{eq}	equivalent diameter, [m]
D_H	horizontal diameter, [m]
D_V	vertical diameter, [m]
D_s	diameter of boiling surface, [m]
f_d	bubble departure frequency, [1/s]
F_B	buoyancy force, [N]
F_{cp}	contact pressure force, [N]
F_{LI}	liquid-inertia force, [N]
F_S	surface tension force, [N]
g	gravitational acceleration, [m/s^2]
h	heat transfer coefficient, [W/m^2 K]
H_L	liquid height, [m]
h_{nc}	natural convection heat transfer coefficient, [W/m^2 K]
h_{exp}	experimental heat transfer coefficient, [W/m^2 K]
h_{fg}	latent heat, [J/kg]
Ja	Jakob number, $\rho_l c_{pl} \Delta T_w / \rho_v h_{fg}$, [-]
K	bubble growth constant in Eq. (3), [m/s^n]
k_{cu}	thermal conductivity of copper, [W/m K]
k_l	thermal conductivity of liquid, [W/m K]
L	characteristic length for natural convection, [m]
l_{ch}	characteristic length for boiling, [m]
m	exponent of Ja in bubble growth law
m_l	liquid mass, [kg]
N	active nucleation site density, [site/m^2]
n	time exponent in the growth law
Nu_{sp}	Single-phase Nusselt number, $Nu_{nc} = hD_s/k_l$, [-]
Nu_b	boiling Nusselt number, $Nu_b = hl_{ch}/k_l$, [-]
P	pressure, [Pa]
$P_{v,R}$	vapour pressure at bubble wall, [Pa]
P_∞	liquid pressure far away from bubble wall, [Pa]
Pr	Prandtl number, [-]
Q_{av}	average heat transfer rate, [W]
Q_{ev}	evaporation heat transfer rate, [W]
Q_{SH}	sensible heat transfer rate, [W]
Q_{LH}	latent heat transfer rate, [W]
Q_{site}	heat transfer rate per nucleation site, [W]
q	heat flux, [W/m^2]
q_{evp}	evaporation heat flux, [W/m^2]
q_{cond}	conduction heat flux, [W/m^2]
r	radial distance, [m]
R	radius, [m]
$R_{b,relax}$	bubble radius due to evaporation from the relaxation layer around the bubble, [m]
R_I	bubble radius due to inertia, [m]
R_{mL}	bubble radius due to microlayer evaporation, [m]
R_{all}	bubble radius due to all mechanisms, [m]
R_c	bubble contact radius, [m]
R_d	departure radius, [m]
$r_{c,exp}$	experimental bubble contact radius, [m]
$R_{e,\ mL}$	radius at end of microlayer evaporation, [m]
R^2	correlation coefficient, [-]
Ra	Rayleigh number, $\beta g(T_w - T_L)D_s^3/\alpha_l \nu_l$, [-]
Re	Reynolds number, $\rho_l 2R(dR/dt)/\mu_l$, [-]
t	time, [s]
$t_{g,mL}$	microlayer evaporation time, [s]
t_d	departure time, [s]
t_{recov}	superheated layer recovery time, [s]
T	temperature, [K]
T_5	Thermocouple no. 5, [K]
T_{sat}	saturation temperature, [K]
T_L	liquid bulk temperature, [K]
T_w	boiling surface temperature, [K]
ΔT_{Ja}	Jackob number superheat, [K]
ΔT_w	wall superheat, (T_w- T_{sat}), [K]
ΔT_{sub}	subcooling, (T_{sat}- T_L), [K]
V_{mL}	microlayer volume, [m^3]
V_v	vapour volume, [m^3]
y	vertical distance, [m]

Greek Symbols

αl	liquid thermal diffusivity, [m^2/s]
β	thermal expansion coefficient, [1/K]
δ_0	initial microlayer thickness, [m]
δ_{th}	thermal boundary layer thickness, [m]
θ	apparent contact angle, [deg]
ν_l	liquid kinematic viscosity [m^2/s]
μ_l	liquid dynamic viscosity [Pa s]
ρ_l	liquid density, [kg/m^3]
ρ_v	vapour density, [kg/m^3]
σ	surface tension, [N/m]

mosiphon system. Bubble growth and dynamics are affected significantly by system pressure. Thus, it is important to study bubble growth at atmospheric and subatmospheric pressures.

Understanding bubble growth is very important for the development of nucleate boiling heat transfer models. For example, Forster and Zuber [1] proposed a model based on micro-convection in the wall thermal boundary layer, see Eq. (1), and used bubble growth velocity (dR/dt) as a characteristic velocity in the definition of the Reynolds number. Additionally, bubble growth models ($R = f(t)$) are needed to estimate the dynamic forces acting on a bubble during its growth period, which can help develop accurate models for the prediction of bubble departure diameter (D_d) and frequency (f_d). These two variables (diameter and frequency) are very important in all mechanistic boiling heat transfer models in which the heat transfer rate due to one nucleation site (Q_{site}) is calculated and the total heat transfer rate is obtained by multiplying Q_{site} by the total number of active nucleation sites N.

$$Nu_b = CRe^a Pr^b \tag{1}$$

It is worth mentioning that there are large discrepancies among the existing nucleate boiling heat transfer models. For the sake of comparison and without going into the details of each model, the present authors plotted the boiling curve in Fig. 1 using 26 models/correlations for water at P = 1 bar, as an example (water was in the database of these models). The figure includes models based on various heat transfer mechanisms such as forced convection induced by bubble agitation, latent heat mechanism, and transient conduction to the liquid layer that rewets the surface after bubble departure (quenching mechanism). Obviously, for a fixed heat flux, there is a big difference in the predicted wall superheat (large differences in the predicted heat transfer coefficient). A reason of this difference could be the discrepancy among researchers on the models used for the prediction of bubble departure diameter and frequency, which are key variables in these mechanistic models. Mahmoud and Karayiannis [2] conducted a review study on pool boiling and included a section on bubble dynamics.

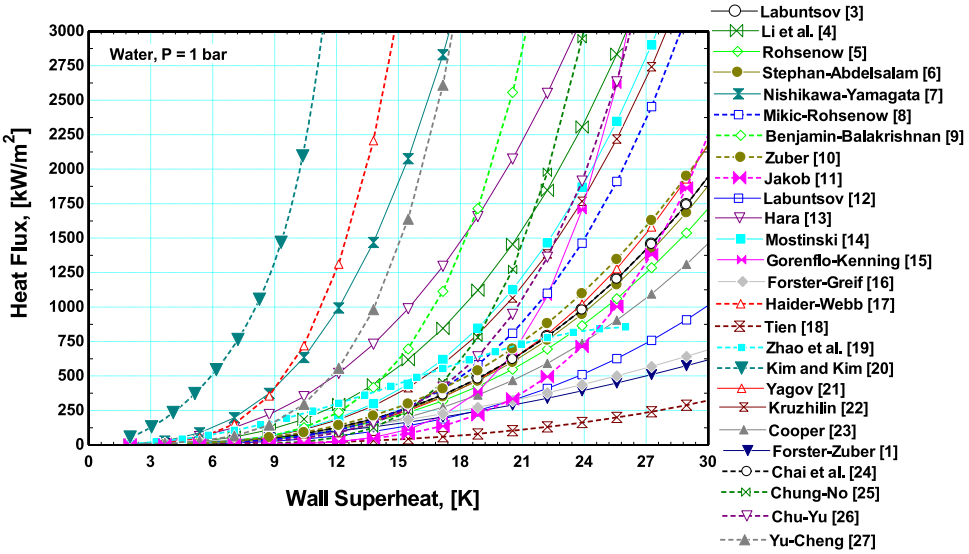

Fig. 1. Discrepancy among 26 heat transfer models/correlations [3–27] for saturated boiling of water at atmospheric pressure.

They plotted the bubble radius versus time from 18 different models/correlations, for water at atmospheric pressure and 10 K superheat, and reported large scatter, e.g. at 14 ms, the radius predicted by one model was about 0.5 mm while that predicted by another model was about 3 mm. It is known that, the heat transfer rate by latent heat, Q_{LH}, for a single nucleation site is proportional to the cube of the bubble departure diameter as given by Eq. (2). Thus, any small error in the prediction of bubble departure diameter can result in a significant error in the prediction of the total heat transfer rate.

$$Q_{LH} = (\pi/6) D_d^3 f_d \rho_v h_{fg} \tag{2}$$

In homogeneous boiling, bubble growth was deemed to be controlled by liquid inertia (inertia-controlled) if the bubble radius follows the relation $R \propto t$ while it was deemed to be controlled by heat diffusion (asymptotic growth) if the radius-time relation follows $R \propto t^{1/2}$. If the exponent of time is larger than 0.5 and less than 1, bubble growth is driven by a contribution from liquid inertia and heat diffusion. Because the inertia-controlled growth dominates the early stage for very short time intervals, it was ignored by many researchers and thus several models were suggested based on the heat-diffusion mechanism. These models were written in the form:

$$R = C Ja^m \sqrt{\alpha_l} t^n = K t^n \tag{3}$$

where C is a factor to account for the bubble curvature, K is a bubble growth constant (empirical or model-based), n is bubble growth exponent, and m is the exponent of Jakob number Ja, which is defined as:

$$Ja = \rho_l c_{pl} \Delta T_w / \rho_v h_{fg} \tag{4}$$

The exponents m and n equal 1 and 0.5, respectively in homogeneous boiling while they may vary in heterogeneous boiling. This is because these models were developed for a spherical bubble with symmetric growth in a uniform superheat while in heterogeneous boiling, bubble shape is not always spherical, the growth is not always symmetric and the superheat is not uniform. It is worth mentioning that bubble growth models will not be included in the current paper, they will be evaluated and discussed critically in a separate publication. Only, the bubble growth characteristics and heat transfer mechanisms will be studied with the help of few models as will be presented in the discussion section. The review below will be limited to saturated boiling of water, which is the test fluid in the current study. The features of bubble growth and the heat transfer mechanisms due to one single bubble will be reviewed and discussed to help understand the reasons of discrepancy among the published bubble growth models.

1.1. Bubble growth characteristics

Bubble growth in saturated boiling of water on metallic surfaces has been investigated by a group of researchers [28–32]. Cole and Shulman [28] conducted the test on a polished zirconium ribbon at P = 0.066 – 0.474 bar and observed that the bubble shape is ellipsoid with a diameter equivalent to a sphere having the same volume, $D_{eq} = (D_H D_V^2)^{1/3}$. It was found that the bubble growth exponent n agreed with the homogeneous models ($n = 0.5$) but the growth constant K was significantly smaller. Additionally, the homogenous models were found to predict the experimental data reasonably well only for $Ja < 100$ if the superheat ΔT_w used in the definition of Ja was modified to $\Delta T_w/2$. It was also concluded that the homogeneous models performed better than the complex heterogeneous models assessed in their study and consequently they correlated their experimental data in a form similar to homogeneous models as given by Eq. (5) but the exponent m of Ja was found to be 0.75 rather than 1.

$$R = 2.5 Ja^{0.75} \sqrt{\alpha_l} t^{1/2} \tag{5}$$

Akiyama et al. [29] studied bubble growth at P = 0.05 – 15 bar on the external surface of a horizontal stainless-steel tube of diameter 8 mm. The bubble shape was observed to be an ellipsoid and the diameter was assumed equivalent to a sphere having the same volume, $D_{eq} = (D_H^2 D_V)^{1/3}$. Note that although the bubble shape is the same as that observed by Cole and Shulman [28], the definition of the equivalent diameter is different. In Akiyama et al. [29], the bubble was assumed symmetric around the vertical axis (axis of revolution) while in [28] it was assumed symmetric around the horizontal axis. It was observed that, as the pressure decreases, the bubble becomes more flattened at the base, especially in the early stages of growth, which was attributed to the increase in bubble growth rate and liquid inertia force which pushes the bubble towards the surface. They also reported that when the bubble shape becomes flat at the base, liquid microlayer forms underneath the bubble and thus there is a possibility for large contribution from microlayer evaporation. On the contrary, when the bubble enters the departure stage (contraction of the contact line), cold liquid

rewets the surface and consequently the liquid inertia force acts in the upward direction (help the bubble to depart), which makes the bubble height larger at low pressures (vertical elongation). The increase in bubble growth rate at low pressures was attributed to the high incipience superheat, the large vapour specific volume, the change in the temperature field around the bubble and the increased contribution from microlayer evaporation. Additionally, the bubble growth constant K and the growth exponent n were found to decrease as the pressure increases (n was larger than 0.5 at sub-atmospheric, about 0.5 at atmospheric pressure, $<$ 0.5 at above atmospheric pressures), e.g. n reached 0.1 at 30 bar for water. Finally, it was concluded that the homogeneous models are valid for nucleate boiling provided that the growth constant K and the growth exponent n are allowed to vary with time and the exponent m of Jakob number should be 0.6.

Stewart and Cole [30] measured bubble growth, up to 20 ms, at 0.048 bar on a polished copper surface of diameter 25.4 mm. The bubble size was observed to be extremely larger than the size of the test section and it was not possible to track bubble growth from nucleation to departure. They visualized the bubble from two sides using two cameras simultaneously and found that the bubble shape is symmetric around the vertical axis, i.e. the 2D projection is a surface of revolution around the vertical axis. Additionally, they estimated the volume-equivalent diameter using two different methods: numerical integration using the 2D bubble profile and simple arithmetic averaging to the horizontal and vertical diameters, $D_{eq} = (D_H + D_V)/2$. It was found that the difference between the two methods was not significant and thus they recommended the arithmetic averaging to get the equivalent bubble diameter. Their results demonstrated that there is a large discrepancy between the experimental data and the prediction from the assessed homogeneous and heterogeneous models. Van Stralen et al. [31] extended the work in [30] through increasing the size of the test section to be able to cover the entire growth period in the pressure range 0.019 – 0.266 bar. It was observed that, for 0.039 $<$ P $<$ 0.266 bar, the bubble shape was hemisphere up to 9 ms and this was considered as inertia-controlled regime, while the heat-diffusion regime was found to be dominant for t $>$ 13 ms. Additionally, as the pressure decreased, the departure diameter and departure time increased while the frequency decreased. For P $<$ 0.079 bar, they observed the following: (i) the waiting time was larger than 10 s and was attributed to the strong cooling of a large area of the surface induced by the large bubble size, (ii) a rapidly growing secondary bubble (vapour column) was observed to penetrate the lower part of the large departing bubble, (iii) a liquid jet with velocity of about 5 m/s was observed in the wake region of the large departing bubble. This jet penetrated the whole bubble (from the bottom to the top) due to the very low pressure in the wake region. The presence of the secondary bubble (vapour column) was attributed to the possible dry patches underneath the large bubble which makes the superheat large enough to initiate a vapour jet similar to film boiling. Gao et al. [32] measured bubble growth on a smooth stainless-steel surface at P = 0.035 – 0.217 bar and observed ellipsoidal bubble shape, symmetric around the vertical axis with diameter equivalent to a sphere having the volume of an ellipsoid, $D_{eq} = \sqrt{D_V D_H}$. Note that this equivalent diameter is different compared to the above studies. It was observed that, at 0.041 bar, the bubble was hemispherical in the first 10 ms then the shape changed to an ellipsoid up to departure. They agreed with van Stralen et al. [31] on observing a liquid jet penetrating the lower part of the bubble. At P = 0.197 bar, the bubble growth phenomenon was the same as P = 0.041 bar except that the bubble size was much smaller and a secondary bubble was observed to penetrate the lower part of the large bubble and a mushroom shape bubble was observed. Note that this secondary bubble phenomenon was observed by [31] at much lower pressure ($<$ 0.079 bar). The measured bubble growth curve indicated the following: (i) for 0.041 bar, the inertia-controlled growth dominated up 40 ms, which is 4 times larger than the duration of 9 ms observed by [31]. (ii) For all tested pressures, the bubble diameter increased rapidly to a constant asymptotic value up to the departure moment. (iii) The bubble growth rate and departure time increased as the pressure decreased, e.g. the departure diameter was about 85 mm at 0.041 bar and decreased to about 40 mm at 0.217 bar. (iv) With increasing pressure, the waiting time decreased from 8 s to 0.2 s while the frequency increased from 0.1 to 4 Hz. The large bubble size and low frequency at lower pressures were attributed to the large vapour specific volume and the large surface tension. The large waiting time was attributed to the large bubble size which displaces large volume of liquid and thus requires long time to be re-heated to the incipience superheat. (v) As the wall superheat increases, the bubble growth rate, the departure size and the departure time increase, which was attributed to a thicker thermal boundary layer around the bubble. It is worth mentioning that van Stralen et al. [31] and Gao et al. [32] inferred the inertia-controlled growth stage without verification. It was based on the bubble shape (hemisphere) in [31] while in [32] it was based on the change of slope in the bubble growth curve, i.e. when the slope changed between the fast and slow growth. This may not be correct as will be discussed in the results section of the current study.

Another group of researchers [33–35] studied single bubble growth on non-metallic surfaces using high-speed video camera, integrated sensors and IR thermography at atmospheric pressure while [36] tested atmospheric and sub-atmospheric pressure. Yabuki and Nakabeppu [33] conducted the test on a silicon substrate coated with SiO_2 from the boiling side with local temperature measurements using Micro-Electro-Mechanical-Sensor (MEMS), Jung and Kim [34] used calcium fluoride substrate coated with indium tin oxide (ITO) from the boiling side and Surtaev et al. [35,36] used a sapphire substrate. The following conclusions can be drawn from these studies: (i) The bubble growth curve followed the relation $R \propto t^{0.6}$ up to about 5 ms then the relation changed to $R \propto t^{0.1}$ in the asymptotic stage as found by [33]. (ii) The departure diameter, growth rate, departure time and microlayer diameter increase as the wall superheat increases and the maximum microlayer diameter was nearly half the maximum bubble diameter, [33,34]. (iii) The bubble radius reaches a maximum value after the complete evaporation of microlayer, at about 10 ms in [33] and 8 ms in [34], then the radius increases slightly or remains unchanged up to departure. (iv) there is a microlayer along with a dry spot at the centre of the contact area and the size of the dry spot increases linearly with time to a maximum value (end of the microlayer evaporation) then it decreased rapidly during the rewetting stage [33,34]. (v) When the experimental data were plotted in a dimensionless form (R/R_d $vs.$ t/t_d), all data collapsed into one single curve regardless of superheat and heat flux as reported by [3]. (vi) Surtaev et al. [36] studied two pressures (0.087 and 1 bar) and reported that the bubble shape was nearly spherical at atmospheric pressure while it was flattened at sub-atmospheric pressure with mushroom shape at departure and a clear vapour stem at the bottom. Additionally, the bubble growth rate, the departure time and departure diameter increase as the pressure decreases. They divided bubble growth into three stages namely, inertia-controlled, transition, and asymptotic stage. In the inertia-controlled growth, the data fitted with $R = Kt$ for a period up to 10 ms at sub-atmospheric pressure and 2 ms at atmospheric pressure. The transition regime occurred only at sub-atmospheric pressure and the data fitted a power law with time exponent of 0.75. In the asymptotic stage, the bubble growth exponent n was found to 0.5 for atmospheric and sub-atmospheric pressure.

The above discussion demonstrated that there is agreement among researchers on the effect of pressure on bubble growth

dynamics. They all concluded that as the pressure decreases, the bubble growth rate, departure size and departure time increase while the frequency decreases. Additionally, the bubble shape is hemispherical and flattened spheroid at sub-atmospheric pressure while it is nearly spherical at atmospheric pressure. Also, some researchers [28,30,31] agreed that the method of estimating the equivalent bubble diameter is not critical. However, some differences among researchers can be summarized as: (i) there is some discrepancy on the duration of the inertia-controlled growth stage where some researchers reported long period and some others reported short periods, which was based only on bubble shape. Inertia-controlled growth was thought to be dominant with hemispherical bubble shape. (iii) some researchers found that the homogeneous and heterogeneous models are not applicable while some others found the homogeneous models are applicable but with some modifications. These deviations may be due to different dominant heat transfer mechanism affecting bubble growth, which will be briefly discussed in the following section.

1.2. Heat transfer mechanisms

This section summarizes the contribution of different heat transfer mechanisms reported by past researchers for saturated boiling of water at atmospheric pressure. There is some inconsistency in naming the various heat transfer processes, i.e. past researchers use different names sometimes for the same heat transfer mode, that can contribute to the on-going debate on this topic. For clarity purposes we try in this first paragraph to list and relate the names to help elucidate possible mechanisms. Some researchers used the terminology “bulk convection”, “transient conduction”, and “quenching mechanism” to describe the same heat transfer mechanism. In fact, the name “bulk convection” was originally given by Han and Griffith [37]. In this mechanism, they assumed that the departing bubble transports periodically most of the wall superheated layer to the liquid bulk and thus cold liquid rushes down towards the hot surface then a new superheated layer forms and transports periodically to the liquid bulk in the same way and that is why it was called “bulk convection”, i.e. wall superheated layer is convected into the liquid bulk periodically. The dominant heat transfer mechanism was assumed to occur by transient heat conduction during the period of re-formation of the superheated layer (re-wetting) and that is why some researchers call it “transient conduction”. Note that evaporation is not included in this mechanism and the only role of the bubble is to transport the superheated layer periodically away from the boiling surface to the liquid bulk. Some other researchers called this mechanism “quenching” due to the periodic cooling of the hot surface, which occurs also by “transient conduction”. The other heat transfer mechanisms in nucleate boiling are clear in the literature and include convection in the spaces among the bubbles (some researchers assumed natural convection and some others assumed forced convection due to bubble agitation) and latent heat transport due to the bubble formation (either due to evaporation from the liquid microlayer underneath the bubble only, or evaporation from the bubble curved surface only or combination of the two). From now on, the mechanism which was called “quenching” in the original papers of other researchers will be called here “transient heat conduction” to use the same and consistent terminology throughout the paper. The mechanisms of convection, will be referred to as natural or forced based on the terminology used by past authors in their papers, if identified as such.

Before discussing the mechanisms, it is important to shed some light on the thermal boundary layer characteristics and the temperature field around the bubble in saturated boiling of water, which is a key variable in bubble growth models. Marcus and Dropkin [38] measured the liquid temperature at vertical locations on a horizontal copper surface using a micro-thermocouple probe in the heat flux range 3.6 – 126 kW/m^2. It was found that the boundary layer was linear only up to $0.57\delta_{th}$ after which it follows a power law. The measured boundary layer thickness was about 0.27 mm at $h = 4000\ W/m^2K$ while it was 0.19 mm at about 8000 W/m^2K. This thickness is much smaller than the size of the water vapour bubble. Ganic and Afgan [39] measured the temperature in the bubble and the surrounding liquid during its growth period using a 120 μm diameter thermocouple probe. The measurements were conducted at five vertical locations above the nucleation site, 0.5, 1.5, 2.5, 3.5 and 5 mm. It was observed that when the thermocouple was at 5.5 mm distance above the nucleation site, it did not detect any thermal wave. When the distance decreased to 3.5 mm above the nucleation site, the thermocouple detected a thermal wave, i.e. the superheated layer seems to be pushed away by the growing bubble. In other words, an envelope of superheated liquid remained around the bubble up to at least 3.5 mm height. It is interesting to note that the velocity of the thermal wave (superheated liquid layer) was nearly the same as the bubble growth velocity. Takeyama et al. [40] measured liquid temperature in the vertical and horizontal directions (0.2, 0.5 mm above nucleation site and 2, 4 mm away from the nucleation site near the surface) using 50 μm diameter thermocouple probe. It was observed that when the probe was at 4 mm horizontal distance from the nucleation site, the probe detected a thermal wave during bubble expansion. Thus, based on bubble size measurements, they concluded that the diameter of the area of bubble influence is 4 times the bubble departure diameter. This area is larger than the value recommended by Mikic and Rohsenow [8] in the heat transfer model that was based on the transient heat conduction mechanism, which was also used extensively by many researchers. When the probe was 0.5 mm above the nucleation site, the probe did not detect any thermal wave (did not detect the superheat). In other words, the superheated layer has been either depleted or the bubble protruded outside the boundary layer, which is in contradiction with the results obtained by Ganic and Afgan [39]. Narayan et al. [41] used non-intrusive rainbow schlieren technique to qualitatively visualize the temperature field around a growing bubble on a glass substrate in subcooled and saturated boiling of water. It was observed that the bubble is surrounded by the superheated layer, which was stretched by the growing bubble during its growth period, and the bubble remained surrounded by the superheated layer even after departure. The estimated wall thermal boundary layer thickness in saturated boiling was about 1.3 mm, which is about 4 times larger than the value measured by [38]. Additionally, they observed a superheated liquid jet in the wake region of the rising bubble. It is obvious from these studies that there are discrepancies about the temperature field around the bubble, which could be a reason for the discrepancies among the bubble growth models and consequently the heat transfer models.

Some researchers studied the heat transfer mechanisms due to single bubble in saturated boiling of water at atmospheric pressure and reported different conclusions. Golobič et al. [42] measured the temperature field underneath a single bubble nucleating on a platinum foil (6 μm thick) using IR camera and did not find any evidence on the presence of microlayer evaporation, evaporation at the three-phase contact line, and enhancement due to the transient heat conduction mechanism. Thus, they recommended further investigations to understand this behaviour. Zupančič et al. [43] studied bubble growth on titanium foil (12.5 μm thick) using high-speed video and IR cameras. They agreed with Globic et al. [42] on that there is no dry spot underneath the single bubble, which was considered as a proof of the absence of microlayer. Contrary to Golobič et al. [42], they concluded that the transient heat conduction mechanism contributed by 90 % while the remain-

ing 10 % was due to the evaporation mechanism. The large contribution from the transient heat conduction mechanism was attributed to the large waiting time (actual values not reported in their study). It is worth mentioning that the waiting time reported by Golobič et al. [42] was 40 ms. Fontana [44] used a high-speed camera and a thin copper disc soldered to a thin layer of constantan and both were soldered to the tip of a copper heating rod. The test section was designed to act as a direct heat flux measurement sensor underneath the bubble. He reported that the contribution due to microlayer evaporation was 60 – 70 % while the remaining 30 – 40 % were due to the transient heat conduction mechanism. Tanaka et al. [45] conducted the tests on sapphire substrate with high-speed video imaging and IR thermography. It was reported that the contribution of microlayer evaporation was about 50 % in the superheat range 13.7 – 16.8 K, transient heat conduction due to rewetting is very small and the rest of the heat was transferred to the bubble by convection. Some other researchers [46–48] studied single bubble growth on glass substrates and found that the contribution of microlayer was 15 – 70 % depending on the superheat (6 – 39 K) as reported by Utaka et al. [46], 14 – 44 % as reported by Hu et al. [47], 17 % by Jung and Kim [34], 9 – 13 % by Narayan and Srivastava [48]. Although Utaka et al. [46] found that the superheat affects the contribution from microlayer, Yabuki and Nakabeppu [33] reported that the superheat did not affect the microlayer contribution.

Although the contribution of the microlayer or evaporation mechanism based on studying one single bubble seems to be large, it might not be the case when heat transfer from the entire boiling surface is studied by considering multiple bubbles. A group of researchers [45,49–51] studied heat transfer mechanisms from the boiling surface by measuring the bubble dynamics and adopting the heat flux partitioning models. Zupančič et al. [49] used the same experimental technique as [43] and conducted the test on zirconium alloy foil with thickness 50 μm at heat flux up to 500 kW/m^2 and studied the heat transfer from the entire boiling surface. They partitioned the heat flux into microlayer evaporation, transient heat conduction and forced convection induced by bubble agitation (estimated by direct local measurements) in the spaces among the bubbles. It was concluded that the contribution of microlayer did not exceed 17 %, the contribution due to forced convection was larger than 80 % and the contribution due to transient heat conduction mechanism was insignificant. The small contribution from the microlayer was attributed to the thin foil (small heat capacity) which did not help evaporate the microlayer completely. Gerardi et al. [50] conducted the tests on sapphire substrate up to about 900 kW/m^2 and also measured the nucleation site density using the IR camera. They used a heat flux partitioning model (turbulent natural convection, transient heat conduction, evaporation) to estimate the contribution of each mechanism. It was concluded that transient heat conduction was the dominant heat transfer mechanism where its contribution was above 70 % at all heat fluxes and the contribution due to evaporation and natural convection (estimated from a correlation for natural convection) mechanisms was less than 30 %. Tanaka et al. [45] conducted the tests on sapphire substrate for heat fluxes up to 600 kW/m^2 and measured the nucleation site density and area fraction of the convection and bubble contact area using the IR camera. Considering the measured area fraction and partitioning the heat flux into microlayer evaporation and liquid heat transfer (convection and transient conduction) indicated that the contribution of microlayer is only about 25 % and the remaining 75 % was due to liquid heat transfer induced by bubble coalescence and agitation. The small contribution of microlayer was attributed to the small area fraction of the bubble contact area (10 % of the total area). It is worth mentioning that the transient conduction was included in the liquid heat transfer part as they could not separate it from the total liquid heat transfer rate during the rewetting period. This result agrees with that reported by Kim and Kim [51] for boiling on silicon substrate. They found that the area fraction of the microlayer is 10 % of the total area and the liquid heat transfer (transient conduction and convection) contributed by 65 – 80 %, while the microlayer contributed by 20 – 25 %.

The above review demonstrates that many fundamental researches has been conducted in the past focusing on understanding single bubble dynamics and heat transfer using transparent or thin-foil substrates. However, they reported different conclusions on bubble growth rate and heat transfer mechanism. Additionally, few researchers focused on studying bubble dynamics on metallic surfaces. Also, in the last two decades, there is a large number of research papers on heat transfer enhancement by surface modification, see Ref. [2]. In these studies, the boiling surface was the top side of a thick copper block and the collected data were used to evaluate existing pool boiling heat transfer correlations/models. As mentioned in the first paragraph, these models depend on bubble dynamic parameters, which in most past studies were measured on transparent and/or thin substrates or on the outer surface of tubes. For example, the bubble growth model by Cooper [52] was based on data obtained using glass and ceramic substrates. Additionally, some researchers agreed with the homogeneous growth theories with exponent $n = 0.5$ while some others reported much smaller value $n = 0.1$ (much slower growth) at the same pressure. Accordingly, more research is still needed to help understand bubble growth on thick copper substrates which may contribute in understanding the reasons of discrepancies among mechanistic heat transfer models. The present study investigates bubble growth on a smooth copper surface at atmospheric and sub-atmospheric pressure using water in saturated conditions. A smooth surface was used to isolate the unclear effects of surface microstructure.

2. Experimental setup

2.1. Boiling chamber and test section

Fig. 2a depicts the schematic drawing of the experimental facility. It consists of the following: (i) rectangular boiling chamber (250 × 250 × 300 mm) made of stainless steel with four transparent visualization windows (158 × 220 mm), (ii) two helical coil heat exchangers (one on the top side of the chamber to work as a condenser and one immersed in the liquid to work as a liquid subcooler), (iii) circulation chiller to supply the cooling water-glycol mixture to the condenser and the sub-cooler, (iv) test section insulation block made of Polyether Ether Ketone (PEEK) that accommodates the copper test piece, see Fig. 2b and 2c, (v) immersion cartridge heater of power 1500 W to control the liquid bulk temperature and conduct liquid degassing before the test, (vi) data logger cDAQ from National Instruments, connected to a PC with Labview software to record the data, (vii) 1.5 kW DC power supply (Electro-Automatik) for supplying the heat to the test section, (viii) High-speed, high resolution camera (Phantom Miro Lab110 – sensor size 20 μm/pixel) with NAVITAR 12X zoom lens system, (ix) two T-type thermocouples for measuring the liquid and vapour temperature and one pressure transducer (Omega, PX319, 0 – 3.5 bar) for measuring the system pressure.

The test section was made of oxygen-free copper and was insulated with the PEEK housing as seen in the exploded view in Fig. 2b and the assembly drawing in Fig. 2c. The copper test piece has a diameter of 30 mm and a height of 42.5 mm, see Fig. 3c. It has five holes of diameter 0.6 mm at 6 mm equal distance along the vertical centreline to insert five thermocouples, and an O-ring shoulder of size 2.5 mm width and 2 mm depth leaving 25 mm diameter as a boiling surface as seen in the CAD drawing in Fig. 3b and c. The test piece was connected to a copper heater block us-

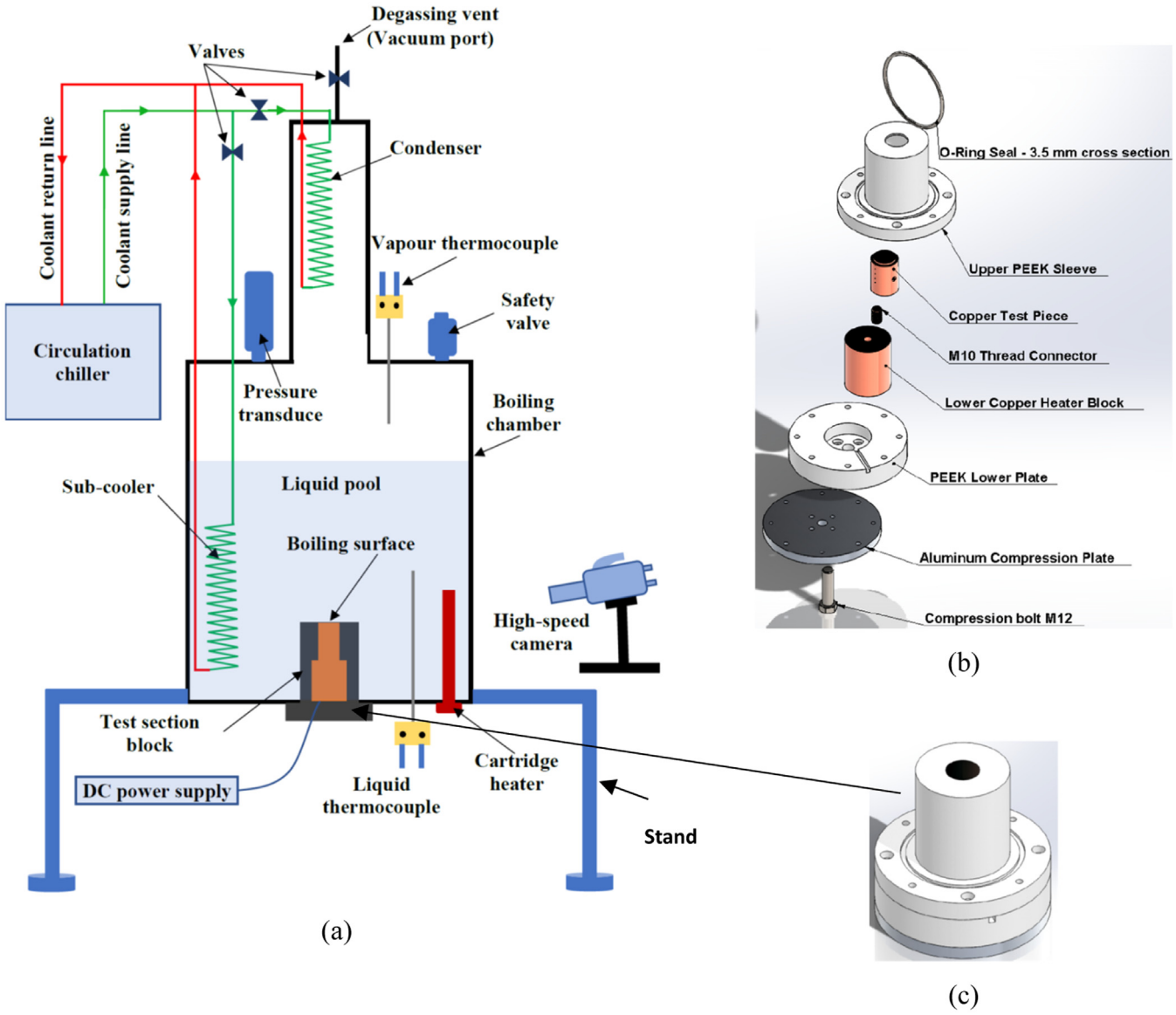

Fig. 2. (a) Schematic drawing of the experimental facility, (b) exploded view of the test section, and (c) the test section assembly.

ing M10 thread connector (made of copper) and the thermal contact resistance was reduced by a thermal paste, see Fig. 3a for the assembly of the test section and the heater block. The heater block has four vertical holes (see Fig. 3b) with diameter 12 mm to accommodate four cartridge heaters (400 W each), which are connected to the DC power supply. The test section was manufactured using High Precision Micro Milling Machine (HERMLE C20U) and the boiling surface was finished by diamond turning machine to obtain a smooth surface. The surface was analysed using Surface Metrology System (NP FLEX-3D) and the S_a value of the tested surface was 49.6 nm. The surface wettability was characterized by measuring the static contact angle for a water droplet at room temperature using contact angle measurement instrument First Ten Angstroms (FTA1000 series). The measured contact angle on the plain copper surface was 85.5^0. This changed marginally to 79.0^0, measured after the boiling experiments.

The temperature reading of the five vertical thermocouples (T5 located at 3.5 mm below the boiling surface) was plotted versus the vertical distance and the gradient was used to calculate the applied heat flux q using Eq. (6). The measured temperature versus distance exhibited linear fitting with a correlation coefficient $R^2 = 0.99$ except the lowest heat flux with $R^2 = 0.96$, which verifies the 1D assumption in calculating q, see Fig. 4. The temperature difference between the wall and the saturation temperature (wall superheat) was calculated using Eq. (7). The saturation temperature was based on the pressure measured using the pressure transducer, which agreed with the measured liquid and vapour temperatures. The wall temperature was calculated using Eq. (8) to account for the temperature drop across the vertical distance between the top side of the boiling surface and the last thermocouple (T5), which is 3.5 mm below the boiling surface. All thermocouples were calibrated and the maximum systematic error in the temperature measurements was ± 0.5 K while the random error was ± 0.003 K, resulting in combined uncertainty of ± 0.5 K. The systematic and random errors were corrected using the best-fit calibration equation. The propagated uncertainty analysis was calculated according to the method given in Coleman and Steel [53] and the highest uncertainty in the heat flux was 7 %.

$$q = -k_{cu}\frac{dT}{dy} \tag{6}$$

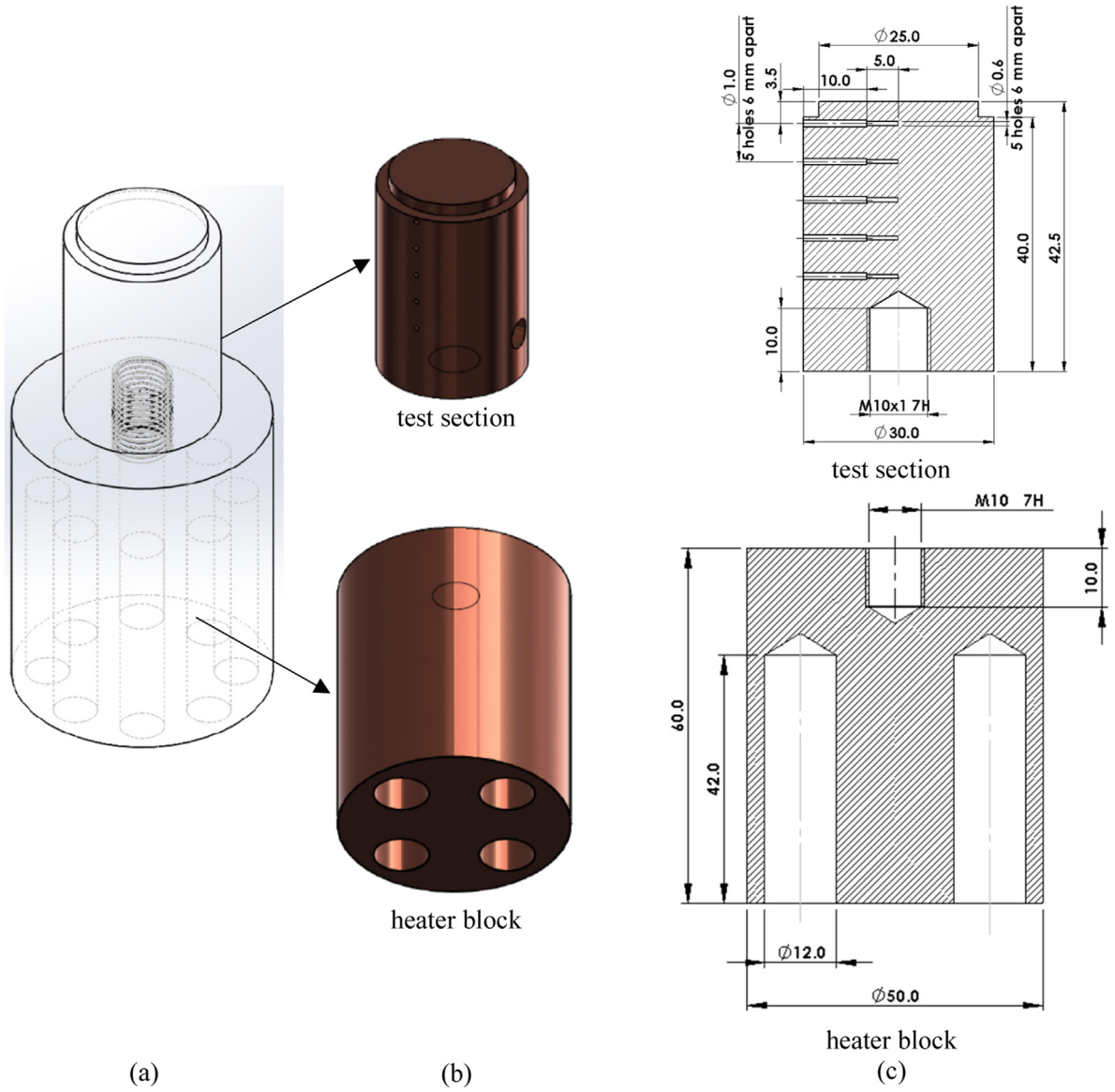

Fig. 3. (a) CAD drawing of the copper test section and the heater block connected with M10 copper threaded connector, (b) CAD drawing for test section (top) and copper heater block (bottom), and (c) 2D drawing of the test section (top) and heater block, (Dimensions are in mm).

$$\Delta T_w = T_w - T_{sat} \tag{7}$$

$$T_w = T_5 - \frac{q\Delta y}{k_{cu}}, \Delta y = 3.5\ mm \tag{8}$$

The experiments were conducted using de-ionized water as a test fluid at atmospheric and sub-atmospheric pressures. The water level above the boiling surface was kept fixed at 130 mm during all the experiments. The thermophysical properties of the fluid required for the calculations were obtained from the Engineering Equation Solver software (EES). All experiments were conducted after degassing the liquid and the boiling surface simultaneously. Liquid degassing was conducted by boiling the liquid vigorously using the 1.5 kW immersion heater and surface degassing was conducted by heating the test section until most of the nucleation sites become active (at about 30 % of the critical heat flux value). The degassing process was deemed to be complete when the measured system pressure becomes equal to the saturation pressure at the measured liquid temperature (the measured liquid and vapour temperature are equal). After degassing, the heat supplied to the test section was switched off until the surface cools down to a temperature below the saturation temperature (all nucleation sites become deactivated). Then, the heat flux was increased gradually in small steps until boiling starts.

2.2. Experimental validation and bubble size measurements

Many researchers validated their experimental system by conducting boiling experiments and comparing the experimental boiling curve with the well-known Rohsenow [5] pool boiling correlation. This approach may not be accurate because boiling depends strongly on the surface microstructure. Additionally, there is no agreement on boiling heat transfer correlations as previously discussed in the introduction section, see Fig. 1. In the present study, experimental system validation was conducted using natural convection single-phase experiments rather than boiling experiments. Fig. 5a depicts the heat flux plotted versus the temperature difference between the surface (T_w) and the liquid (T_L). The results were compared with the natural convection correlation reported in

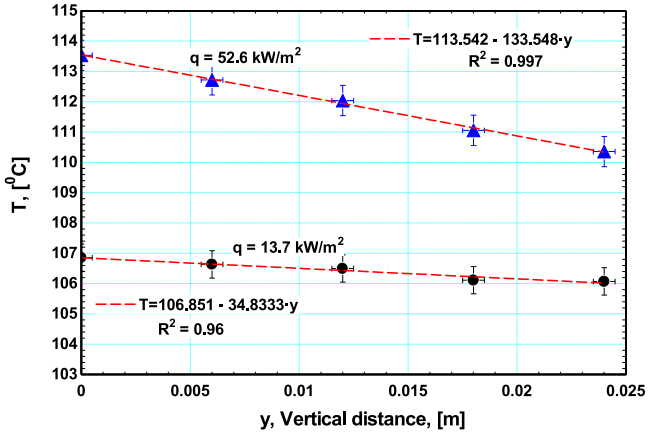

Fig. 4. Measured temperature versus the vertical distance from the top surface.

Bergman et al. [54], see Eq. (9). It is obvious that there is a good agreement between the measurements and the prediction with average deviation of 8.8 %, which verifies the accuracy of the experimental measurement system.

$$Nu_{sp} = \begin{cases} 0.54Ra^{1/4} & 10^4 \le Ra \langle 10^7, \ Pr \rangle 0.7 \\ 0.15Ra^{1/3} & 10^7 \le Ra < 10^{11}, \ all \ Pr \end{cases} \quad (9)$$

As discussed in the introduction section, researchers defined the equivalent bubble diameter in different ways depending on the assumed axis of symmetry. Some other researchers [35] measured the bubble diameter from the bottom side of a transparent substrate, which may not be accurate especially when the bubble is not spherical in shape (bubble vertical elongation was not considered). Although some researchers [28,30,31] reported that the method of estimating the equivalent bubble diameter is not critical, it is important to verify this conclusion in the present study. It is worth mentioning that, in the present study, the camera is tilted by an angle of 17^0 to the horizontal and this angle was kept fixed in all experiments. The tilt angle was measured directly using the camera tilt mechanism. Additionally, it was not possible to insert a standard scale bar near the boiling surface inside the boiling chamber to be used as a reference scale for the bubble size measurements. Therefore, a careful calibration was conducted to the high-speed camera tilted with an angle of 17^0 at fixed lens magnification of 0.58x. The calibration was conducted using a standard ball bearing of diameter 12.7 mm measured using a micrometre with an accuracy of ± 1 μm. Fig. 5b depicts a picture for the standard ball taken by the high-speed camera at lens magnification 0.58x and tilt angle 17^0 (the same as the experiments). All measurements in the picture was conducted using ImageJ software. It is worth mentioning that the camera tilt should not affect the horizontal dimension (front view) while the height of an object is expected to be slightly shorter than the real height. Based on that, the horizontal diameter of the standard ball bearing was used to calibrate the pixel size in μm which gave 22.6 μm/pixel. It is also obvious in Fig. 5b that the vertical diameter is 4.5 % smaller than the horizontal diameter due to the effect of camera tilting angle. In other words, the camera tilt with the angle used in the present study did not have a significant effect on the bubble size measurements. To estimate the error in the measured diameter, the diameter of the standard ball in Fig. 5b was calculated using two different methods: area-equivalent diameter (diameter of a circle equivalent to the projected frontal area) and volume-equivalent diameter estimated by integration (diameter equivalent to a sphere having the same volume). Based on the projected area, the value of the diameter was found to be 12.63 mm, which is 0.6 % smaller than the real diameter. The volume was calculated by numerical integration, through dividing the projected area into small horizontal discs with height 100 μm. On doing so, the numerically calculated volume was found to be 1031.1 mm^3 while the actual volume of the standard ball was 1072.53 mm^3. Thus, the calculated volume-equivalent diameter was found to be 12.53 mm which is 1.5 % smaller than the diameter of the standard ball. Accordingly, the equivalent diameter can be estimated in the present study with an error smaller than 2 %. The effect of the method of estimating the equivalent diameter (volume-equivalent, area-equivalent, average diameter) was investigated in this study for a bubble at sub-atmospheric pressure (more flattened shape). Fig. 6 depicts the bubble growth curve at 0.15 bar with the radius estimated using the three different methods. The figure demonstrates that there is no significant difference between the method of es-

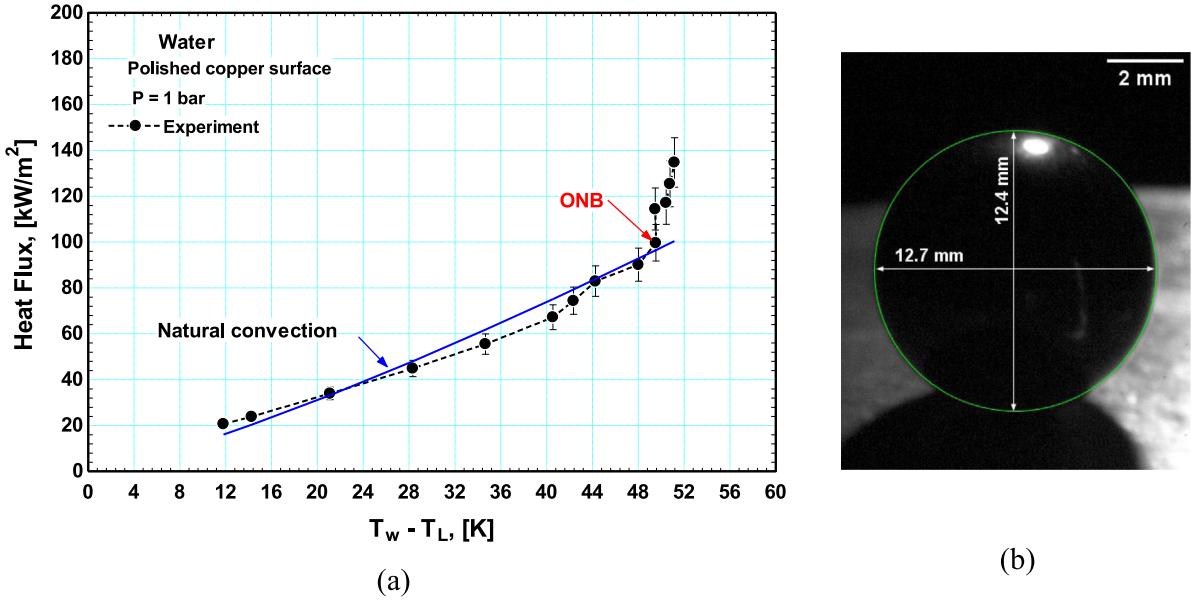

Fig. 5. System validation and bubble measurements: (a) Experimental system validation using single-phase natural convection and (b) calibration of the pixel size of the high-speed camera (tilted by angle 17^0) using standard ball bearing of size 12.7 mm.

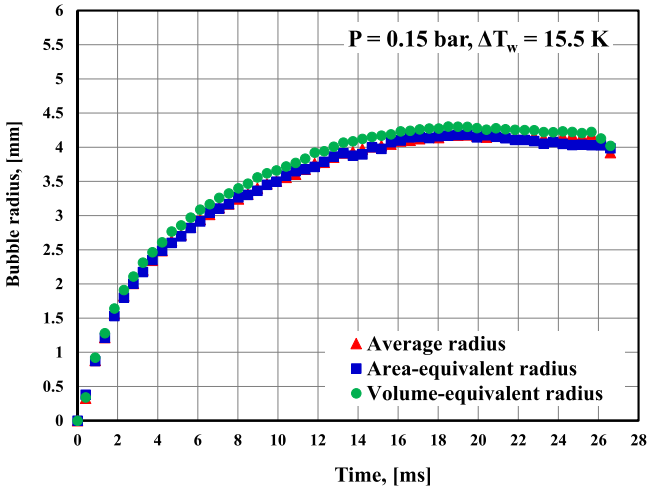

Fig. 6. Difference between equivalent bubble diameter estimated using three different methods for bubble growth at 0.15 bar.

timating the bubble equivalent diameter and the difference between all methods (average diameter, area-equivalent and volume-equivalent) is less than about 5 %. This analysis agreed with the conclusion given by Stewart and Cole [30] as aforementioned in the introduction section. Accordingly, the area-equivalent diameter was used in the current study in the early stages of growth when the bubble is small and is not sufficient to use integration and in the other stages of growth, the volume equivalent diameter was used.

3. Results and discussion

This section presents the experimental results of bubble growth in saturated boiling of de-ionized water on a smooth cooper surface at atmospheric (1.01 bar) and sub-atmospheric pressure (0.15 bar). It is worth mentioning that the bubbles investigated in the current study were nucleated from the random cavities created by the roughness that still exist even on smooth surfaces. Additionally, it was difficult to track the nucleation characteristics from the same active nucleation site at different values of superheat. This is because the nucleation site, which was active at the lowest superheat, becomes either suppressed by the activation of other neighbouring sites or coalesced with other active sites or other neighbouring nucleation sites become active and block the view of the camera from reaching the originally tracked site. Thus, in the present study, an active nucleation site was selected randomly for analysis such that there is no horizontal or vertical coalescence. In conclusion, the selected nucleation site may not be the same for all values of the measured average superheat. Additionally, it is very common in boiling to observe that bubble growth rate, departure diameter and frequency can vary from cycle to cycle for the same nucleation site at the same measured average superheat. This may be due to variations in the local superheat, which is not measured in all similar experimental setups. Accordingly, the cycle to cycle variation has been investigated and discussed in this study. It is worth mentioning that the objective of this paper is not to evaluate the existing bubble growth models. Only three models will be used to help discuss and understand the bubble growth mechanisms at atmospheric and sub-atmospheric pressure.

3.1. Bubble growth at atmospheric pressure

3.1.1. Bubble growth curve

In this section, the discussion of the bubble growth characteristics will be performed for one ebullition cycle at P = 1.01 bar, ΔT_w = 9.4 K, and $q = 17.6$ kW/m^2. Fig. 7 depicts the frame by frame image sequence captured using the high-speed video camera at a frame rate of 2182 f/s (time resolution 0.458 ms). The cycle starts from the frame just before the appearance of the studied bubble and this frame was designated an arbitrary reference time 0 ms, as seen in the first picture. The arrow in this picture refers to the location of the studied nucleation site. Based on the bubble shape, the figure illustrates that the bubble passes through three stages during its growth period. The first stage dominated nearly the first 5 ms and the bubble shape was nearly a flattened spheroid with the size of the bubble and contact area increasing with time. In the second stage (5 – 7 ms), the bubble shape changed from the flattened spheroidal shape into nearly a spherical shape. In the final stage (above 7 ms), the bubble exhibited vertical stretching and the bubble contact area contracted rapidly until a thin cylindrical vapour stem (neck) appeared at 11.92 ms (just before departure). After departure, the bubble became flattened from the bottom side. In this cycle, the bubble departure diameter was 2.932 mm, the departure time was 12.37 ms, the waiting time was 5.05 ms and thus the bubble generation frequency ($1/(t_{wt}+t_d)$) from this site was 57.4 Hz. The departure time is defined here as the time period measured from the appearance of the nucleating bubble to the moment of departure. This behaviour has been reported by many researchers [33,34,36,55] as discussed in the introduction section. Johnson et al. [56] studied bubble growth in saturated pool boiling of water on a polished metal strip (Chromel-P). They observed three different shapes (hemispherical, spheroid, and spherical) and attributed the difference in shape to the relative importance of the forces acting on the bubble. It was reported that the hemispherical shape occurs when the liquid inertia force is much larger than the surface tension force while the spherical shape occurs when the surface tension becomes larger than the liquid inertia force. The spheroidal shape is an intermediate between the hemispherical and the spherical shape and occurs when the liquid inertia is slightly larger than the surface tension force. Additionally, they reported that the bubble with a spherical shape can occur when the waiting period is very short and this was attributed to the local cooling effect at the nucleation site and the believe that there is not enough time for the complete recovery of the superheated boundary layer after bubble departure. This leads to lower vapour pressure at the boiling surface and to a slow bubble growth (small liquid inertia) and consequently makes the surface tension force larger than the liquid inertia force.

To quantify the forces acting on the bubble during the whole growth period shown in Fig. 7 and understand the growth mechanism, the bubble growth curve (radius versus time) is needed. As mentioned above, the time resolution (difference between consecutive frames) is 0.458 ms and the reference zero time (when the bubble radius is zero) in the first picture in Fig. 7 may not be accurate. To plot the bubble growth curve accurately, the actual zero time is needed (it is somewhere between the first and second frames in Fig. 7). This zero time may result in a significant error, especially when the pictures are captured at a low speed. For example, if the camera speed was 500 f/s, the maximum error will be 2 ms (about 20 % error for a departure time of 10 ms). This zero-time shift was discussed by Johnson et al. [56]. To consider the effect of zero time in the present study, the data were plotted from the time at which the bubble appears (the second picture in Fig. 7) up to the departure time and the best fit polynomial equation was obtained. This equation was extrapolated to find the time corresponding to the zero radius (intersection of the curve with the time axis) which was found to be 0.328 ms (note that it must be smaller than or equal to the time difference between each frame). Thus, the effect of the actual zero time corresponds to shifting each data point in the *R-t* plot to the left by a certain time interval (in this case 0.13 ms) as seen in Fig. 8a, which

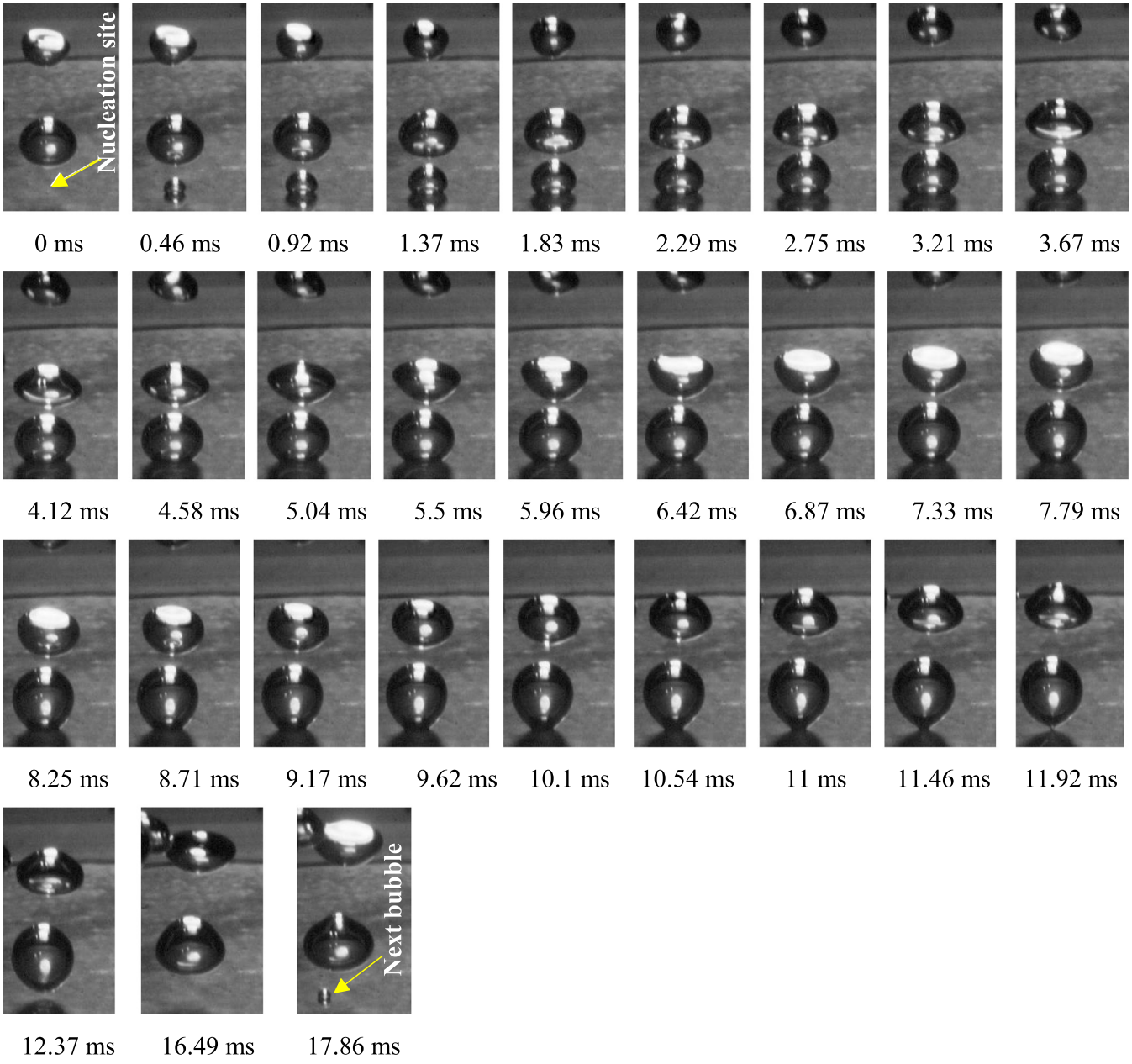

Fig. 7. Bubble growth during one ebullition cycle at P = 1 bar and $\Delta T_w = 9.4\ K$.

shows part of the growth curve (just for clarity). Thus, if this error is large, it might affect the conclusion on the performance of bubble growth models. All bubble growth curves presented in the current study are corrected for the zero-time shift. Fig. 8b depicts the measured bubble radius plotted versus time up to departure for the cycle in Fig. 7. It is obvious that the curve exhibits a clear change in slope after about 3.5 ms indicating that there are two stages of growth namely, rapid growth in the period below 3.5 ms and slow growth in the period above 3.5 ms. It is worth noting that the bubble radius at the end of the first stage (3.5 ms) is 1.28 mm, which is about 88 % of the departure radius (1.47 mm). Thus, this stage can be roughly called the "growth stage". The size of the contact area underneath the bubble is another important factor in quantifying the contribution from the microlayer evaporation and estimating the surface tension force, as will be discussed later. The radius of the contact circle between the bubble and the boiling surface was also included in Fig. 8b. It is worth mentioning that it is not possible to track the exact three-phase contact line in the contact region using the high-speed camera looking from the side view. Accordingly, the measured contact radius in the present study is the apparent radius, seen by the camera. It is obvious from Fig. 8b that the apparent contact radius increased rapidly, in a similar manner as the bubble radius, up to 3.5 ms, where it reached its maximum value then it started decreasing continuously to zero at the departure moment. In other words, the contact radius exhibits two stages in a similar manner as the bubble growth curve. In the first stage, the apparent contact line expands rapidly while in the second stage it contracts slowly at the beginning then rapidly up to zero at departure. The behaviour of the apparent contact radius was reported and explained by some researchers such as Kim et al. [57] and Allred et al. [58]. They reported that the three-phase contact line passes through three stages during the bubble growth period. In the first stage, the contact circle expands with the dynamic receding contact angle until it reaches its maximum size. In

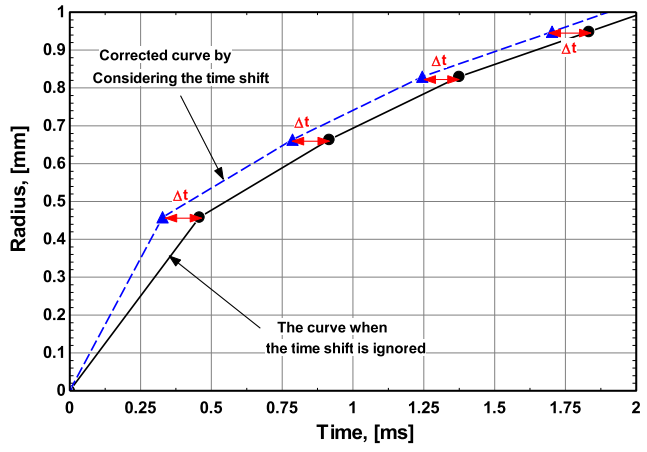

(a)

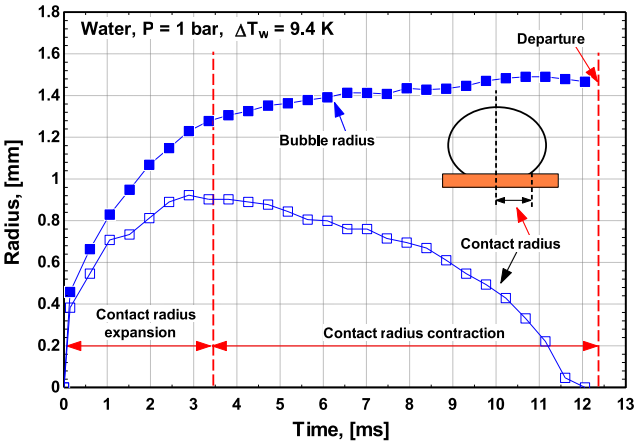

(b)

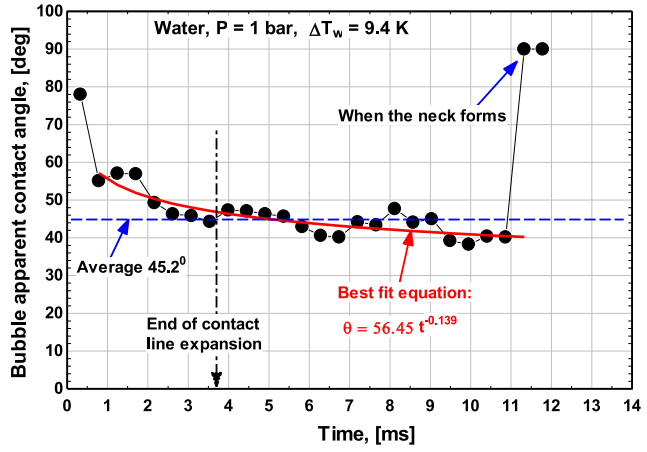

(c)

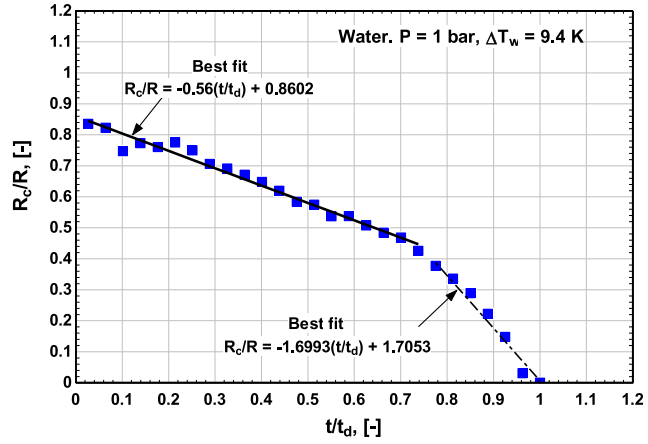

(d)

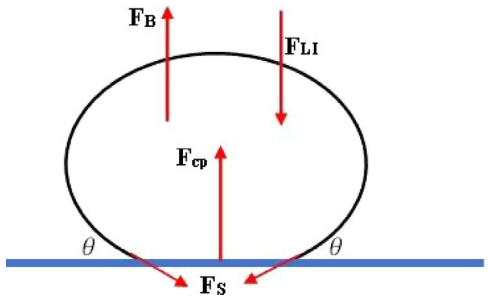

(e)

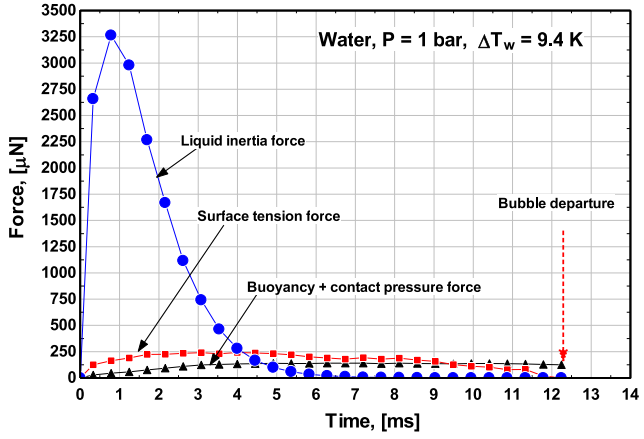

(f)

Fig. 8. Bubble growth at P = 1 bar and $\Delta T_w = 9.4\ K$: (a) effect of zero-time shift, (b) bubble radius and apparent contact radius versus time, (c) apparent contact angle versus time, (d) dimensionless apparent contact radius versus dimensionless time, (e) schematic showing the forces acting on the bubble, (f) forces acting on the bubble (liquid inertia, surface tension, buoyancy and contact pressure).

this stage, the liquid is pushed radially away from the nucleation site. In the second stage, the size of the contact circle remains unchanged for a short period and the contact angle increases from the receding to the advancing contact angle, this was also called the "contact line pinning stage". In the third stage, once the contact angle reaches the advancing angle, the contact circle starts shrinking with time and thus the liquid at the surface flows towards the nucleation site, which is usually called the "rewetting stage". It is worth noting that the measured contact radius in Fig. 8b depicts two stages as mentioned above without the middle stage (contact line pinning). This indicates that the contact angle hysteresis is not significant during this bubble growth cycle. To get an idea about

Table 1
Instantaneous forces acting on the bubble during its growth period taken from [59].

Force	Equation	Comments
Buoyancy force, F_B	$(\rho_L - \rho_v)g\frac{4}{3}\pi R^3$	The radius R was the measured instantaneous radius
Surface tension forces, F_S	$-2\pi R_c\sigma \sin\theta$	The contact radius r_c and contact angle were the measured instantaneous values
Contact pressure force, F_{cp}	$\pi R_c^2 \frac{2\sigma}{5R}$	The contact radius r_c was taken directly from the experiment
Liquid inertia force (growth force), F_{LI}	$-\rho_L\pi R^2(\frac{3}{2}C_s\frac{dR}{dt} + R\frac{d^2R}{dt^2})$ $C_s = 20/3$	The radius, velocity and acceleration were taken from the experimental data

the measured apparent dynamic contact angle, the angle was measured directly from the image sequence using the ImageJ software and the results are plotted in Fig. 8c. As seen in the figure, the contact angle decreases from a high value ($< 90^0$) when the bubble appeared at time 0.46 ms then it decreased slowly with time during the whole growth period except near departure when a cylindrical neck forms with an apparent contact angle of about 90^0. The best fit equation is also shown on the figure excluding the end points ($\theta = 56.45t^{-0.139}$). Inspecting the figure, one can conclude that the contact angle after about 2 ms is fluctuating around an average value of 45.2^0 with $\pm\ 5^0$. In other words, the contact line expands and contracts with nearly the same angle indicating insignificant contact angle hysteresis and hence the absence of the pinning effect (the intermediate stage). Fig. 8d shows the contact radius plotted in a dimensionless form as R_c/R versus t/t_d and demonstrates that the dimensionless radius smaller than one at the beginning indicating that the bubble shape was not a perfect hemi-sphere (the ratio should be one for hemispherical bubbles). Additionally, the data was found to fit with two linear segments with a strong change in slope after dimensionless time of about 0.73. This is due to the increased acceleration of the contact line during the re-wetting stage near the time of departure.

The forces acting on the bubble are described with the help of the schematic in Fig. 8e and the actual relationships are given in Table 1. In order to quantify the forces acting on the bubble during its growth period, the forces are calculated based on the method adopted by Bucci et al. [59] and the result is shown in Fig. 8f. The liquid inertia, the surface tension, the buoyancy and the contact pressure forces are included in the figure. The liquid inertia force can be upward or downward depending on the bubble growth velocity and acceleration, the surface tension is always a downward force while the contact pressure and buoyancy forces are always upward, therefore they were added together in Fig. 8f. Generally, when the bubble is expanding and there is no condensation, the liquid inertia force is always downward and thus it pushes the bubble towards the surface. When there is strong condensation, as will be the case in subcooled boiling or at certain conditions in sub-atmospheric pressure, the liquid inertia is negative (downward) at the beginning in the bubble growth stage and changes its direction (upward) after the bubble reaches its maximum size and shrinks due to condensation. The contact radius and the apparent contact angle required for the calculation of the surface tension force and the contact pressure force were taken directly from the experimental data. It is worth mentioning that the viscous drag, the vapour inertia, and the lift forces were also evaluated and the values were very small (near the zero line) and thus were removed from the figure for clarity. The figure shows that the liquid inertia force is much larger than the other forces in the first 4 ms and tends to zero at time greater than 4 ms. This explains the flattened spheroidal bubble shape in Fig. 7 at the beginning of bubble growth. In the intermediate stage (4 – 8 ms), the liquid inertia force diminished and the surface tension force was slightly larger than the buoyancy force which explains the gradual change into the spherical shape. In the last stage (> 8 ms), the combined buoyancy and contact pressure force exceeded the surface tension force and thus the bubble stretched in the vertical direction and the thin cylindrical neck has been formed immediately before departure. Thus, it may be concluded that at atmospheric pressure, the departure diameter can be predicted using a static force balance between the buoyancy and the surface tension force (ignoring the contact pressure force). To verify this premise, a static force balance is conducted according to Eq. (10). This balance should be at the moment when the two forces are nearly equal. Based on Fig. 8f, the surface tension and buoyance forces are equal at 9.5 ms and thus the balance should be conducted at this moment, which is 3 ms before departure.

$$(\rho_l - \rho_v)g\frac{4}{3}\pi R^3 = 2\pi R_c\sigma\ \sin\theta \tag{10}$$

The contact radius and the contact angle were obtained from the experimental data. From Fig. 8b, at 9 ms, the ratio between the contact radius and bubble radius R_c/R is equal to 0.43 and from Fig. 8c, the apparent contact angle at 9 ms is 45^0. Substituting these values in Eq. (10), the departure radius will be 1.67 mm, which is 13% larger than the measured value (1.48 mm). The reasonable agreement between the measured and the calculated value verifies the premise that static force balance between buoyancy and surface tension forces is sufficient to predict departure diameter at atmospheric pressure. It is interesting to note that using Fritz [60] model given by Eq. (11) with the measured contact angle 45^0 at 9 ms results in departure radius of 1.16 mm which is 21.6 % smaller than the measured value. For Fritz model to fit exactly the measured value, the contact angle should be 57^0 rather than 45^0. The recommended contact angle in the present study (45^0) agrees with Stephan-Abdelsalam [6] who recommended the same value to be used in Fritz model to predict the departure diameter for water. In conclusion, the contact angle used in Fritz model is not a variable and is not the static contact angle. The measured static contact angle in this study is 85.5^0 and if it was used in Eq. (11), the departure radius will be 2.2 mm (51 % larger than the measured value). In other words, Fritz model did not consider the effect of surface wettability and hence a varying contact angle.

$$R = 0.5 \times 0.0208\theta\sqrt{\frac{\sigma}{g(\rho_l - \rho_v)}} \tag{11}$$

3.1.2. Bubble growth mechanism

It is important to understand whether bubble growth in heterogeneous boiling is controlled by liquid-inertia or by heat diffusion (asymptotic growth). Based on the change in slope of R *vs.* t plot in Fig. 8b, one may conclude that bubble growth is controlled by liquid inertia due to the rapid growth in the first 3.5 ms and it is controlled by heat diffusion after that, due to the slow growth in the asymptotic stage. Inferring the growth mechanism qualitatively based on the change in slope only may not be accurate. As mentioned in the introduction section, in homogeneous bubble growth models, the inertia-controlled growth was deemed when the radius follows a linear relation ($R \propto t$) while it is heat diffusion-controlled growth if the relation is a power law ($R \propto t^{1/2}$). To investigate the bubble growth controlling mechanism, the bubble growth curve in Fig. 8b was segregated into two segments in Fig. 9a. The inertia-controlled growth can be studied

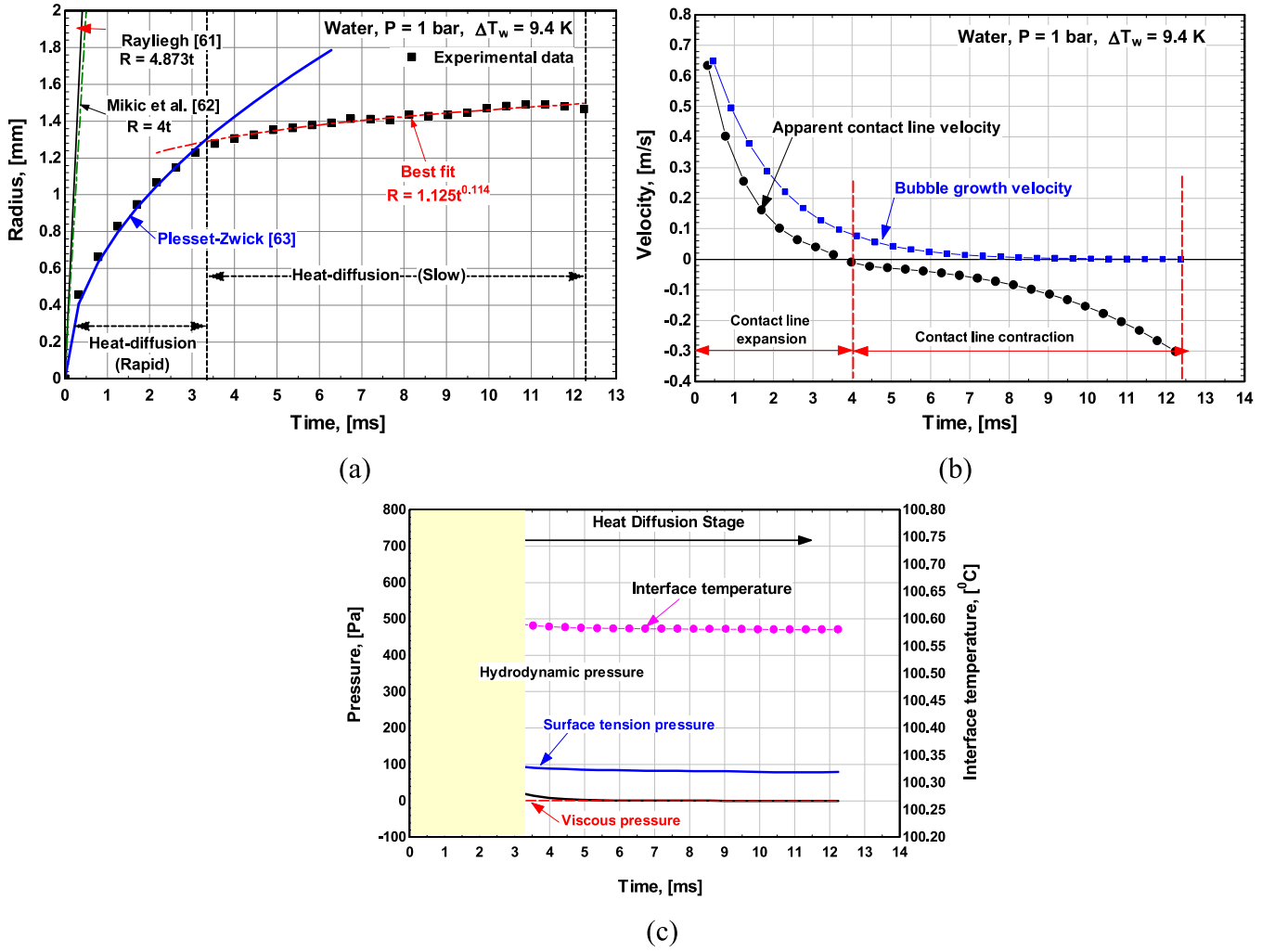

Fig. 9. Understanding bubble growth mechanisms: (a) Bubble radius compared with inertia and heat diffusion growth models, (b) Bubble growth velocity and apparent contact line velocity, (c) Pressure terms in the extended Rayleigh equation (Eq. (15)) and the predicted interface temperature.

using the Rayleigh [61] equation defined by Eq. (12), which can be reduced to $R = 4.873t$ when the measured average superheat ($\Delta T_w = 9.4K$) and fluid properties at the system pressure were substituted into the equation. This equation was modified by Mikic et al. [62] to account for heterogeneous boiling as defined by Eq. (13), which can be written in a similar form as $R = 4t$. The two equations Eq. (12) and ((13)) are plotted in Fig. 9a which demonstrates that the first data point at time 0.328 ms seems to be very near to the inertia-controlled growth curve. However, the predicted value by the two equations is 190 – 250 % larger than the measured value, which indicates that none of the measured values follow the inertia-controlled growth mechanism for time period down to 0.328 ms. To study the heat diffusion growth mechanism, the experimental data were compared with the homogeneous bubble growth model given by Plesset and Zwick [63] and defined by Eq. (14). As seen in Fig. 9a, the model exhibited excellent agreement with the experimental data up to 3.5 ms, indicating that the superheat may be uniformly distributed around the bubble during this period. It is interesting to note that when the experimental data in the time interval up to 3.5 ms (first segment) were fitted into a power law, the relation was found to be $R = 0.751t^{0.44}$, which is comparable to the Plesset-Zwick model $R = 0.71t^{0.5}$. The figure also shows that the second segment of the curve (slow growth stage from 3.5 ms to departure) can be fitted into a power low but with very small time exponent $R = 0.125t^{0.114}$. Thus, it can be concluded that the bubble described in Fig. 9a grows due to heat diffusion along the entire growth period (from 0.33 ms to departure) according to two stages: (i) rapid growth stage up to 3.5 ms in which the superheat seems to be uniform, and (ii) slow growth stage from 3.5 ms up to departure in which the superheat seems to be not uniform. It is also obvious that the Plesset-Zwick model (developed for asymptotic growth stage in homogeneous boiling) cannot predict the slow growth stage in heterogeneous boiling, i.e. cannot account for the nonuniform superheat.

$$R = \left[\frac{2}{3}\frac{\rho_v h_{fg}\Delta T_w}{\rho_l T_{sat}}\right]^{1/2} \mathrm{t} \tag{12}$$

$$R = \left[\frac{\pi}{7}\frac{\rho_v h_{fg}\Delta T_w}{\rho_l T_{sat}}\right]^{1/2} \mathrm{t} \tag{13}$$

$$R = \sqrt{12/\pi}Ja\sqrt{\alpha_l t} \tag{14}$$

Another approach to infer the bubble growth mechanisms is the analysis of the extended Rayleigh equation cited in Ref. [63] and given by Eq. (15), which relates the pressure difference across the interface (left-hand side) with the right-hand side, liquid inertia (first term), surface tension (second term) and viscous stresses (third term). This equation was derived from the momentum and

mass conservation principles for a spherical bubble in homogeneous boiling. It can be used in this section to get an idea about the growth mechanisms or identify whether there is a difference or not between homogeneous and heterogeneous bubble growth. The bubble growth velocity dR/dt and acceleration d^2R/dt^2 required for this analysis were obtained directly from differentiating the best fit equation of the measured bubble growth curve. For example, Fig. 9b depicts the growth velocity along with the velocity of the contact radius, which may help in estimating the convection heat transfer coefficient during the expansion (de-wetting) and contraction (rewetting) stages. It demonstrates that the bubble growth velocity decreased rapidly from about 0.65 m/s at the beginning to nearly zero at about 8 ms and remained unchanged up to departure. On the contrary, the contact line velocity decreased rapidly from 0.63 m/s and reached about zero value at time around 4 ms then the velocity became negative when the direction of motion was reversed due to the contraction of the contact line during the rewetting stage and the velocity was about 0.3 m/s near departure.

$$P_{v,R} - P_\infty = \Delta P = \rho_l \left[R\frac{d^2R}{dt^2} + \frac{3}{2}\left(\frac{dR}{dt}\right)^2 \right] + \frac{2\sigma}{R} + 4\mu_l \frac{1}{R}\frac{dR}{dt} \quad (15)$$

Each term in the right-hand side of Eq. (15) is plotted in Fig. 9c based on the measured bubble radius, growth velocity and acceleration. The figure shows that the hydrodynamic pressure (1st term on the r.h.s) was nearly twice the surface tension pressure at the beginning then it decreased rapidly to nearly zero at 4 ms. The surface tension pressure decreased rapidly in the first 3 ms and remained nearly unchanged during the rest of the growth period. The figure also demonstrates that the viscous term is nearly zero and can be ignored. Robinson and Judd [64] conducted a numerical study for hemi-spherical bubble growth in nucleate boiling and explained in detail the different mechanisms of bubble growth which includes four stages namely, surface tension dominated stage, transition stage (surface tension and inertia), inertia dominated stage and heat diffusion dominated stage. The first two stages dominate for short time periods (in the order of microseconds), which cannot be detected in the current study because the time resolution is 0.46 ms. They reported that the heat diffusion-controlled growth regime starts when the surface tension pressure reaches its minimum value and remains unchanged and when the hydrodynamics pressure becomes nearly zero. In that case the pressure difference ΔP in Eq. (15) will be zero, i.e. the vapour pressure equals the liquid pressure at the interface. Thus, there will not be a temperature gradient at the interface induced by the dynamic effects and for the bubble to grow, a second mechanism should take over, i.e. the heat diffusion mechanism. To apply this physics in the current study, the liquid-vapour interface temperature was predicted using the vapour pressure estimated from Eq. (15) with the liquid pressure P_∞ at the interface including the hydrostatic pressure term ($\rho_l g H_L$), where H_L is the liquid height in the boiling chamber. This temperature is included also in Fig. 9c and indicated that the temperature dropped rapidly in the first 4 ms (steep temperature gradient at the interface) then remained nearly unchanged indicating zero temperature gradient (end of evaporation due to dynamic effects). Based on this analysis, the heat diffusion-controlled growth (asymptotic regime) stage started after about 4 ms while for time below 4 ms, the dynamics effects are dominant (inertia and surface tension). This result contradicts the conclusion based on in the power law fitting in Fig. 9a, which indicated that the exponent of time is 0.44 (a feature of heat diffusion regime). It is worth mentioning that if inertia and surface tension constituted the controlling factor in bubble growth, the expected exponent of time must be greater than 0.5 (the upper bound is 1 in the inertia-controlled regime). Thus, it may be concluded that either the assumptions adopted in the dynamic equation, which is applicable for spherical bubble growth in homogeneous boiling, may not be valid for heterogeneous boiling or the two mechanisms (inertia and diffusion) exist but diffusion effects exceed the dynamic effects significantly.

3.1.3. Heat flow into the bubble

Based on the conclusion from the above discussion, the bubble grows by heat diffusion rather than dynamic effects. Thus, this section discusses how the heat flows into the bubble, i.e. was it through the curved surface or through the liquid microlayer underneath the bubble? Two models are used in this discussion namely, the homogeneous bubble growth model by Plesset and Zwick [63] defined by Eq. (14) above and the microlayer evaporation model given by Cooper [52] and defined by Eq. (16) below. Fig. 10a shows the experimentally measured bubble growth radius versus time compared with the two models (see curve 1 and 2). The figure demonstrates that both models predict the bubble radius very well during the early stage (up to 3.5 ms), which is corresponding to the end of the contact line expansion as discussed above (see Fig. 8b). After 3.5 ms, both models significantly overpredict the experimental data. The question is: why the homogeneous model (Eq. 14) which was based on a uniform superheat around a spherical bubble agrees very well with a model which was based on evaporation from the contact area underneath the bubble (Eq. 16)? To answer this question, the Cooper [52] microlayer evaporation model should be investigated first. This model suggested that the bubble grows as a hemisphere due to evaporation of the liquid trapped in a microlayer underneath the bubble with initial thickness δ_0. To determine the initial microlayer thickness, Cooper conducted analysis based on the hydrodynamic theory assuming that the bubble grows with a known power law ($R = C_1 t^n$), which is similar to the homogeneous heat-diffusion models. In other words, the bubble growth model was an input parameter in determining the initial microlayer thickness. On doing so and assuming $n = 0.5$, Cooper obtained an analytical expression for the initial microlayer thickness $\delta_0 = C_2\sqrt{\nu_L t}$ with an empirical constant $C_2 = 0.8$. Thus, it is not surprising that the obtained final expression for the bubble radius in Eq. (16) is similar to the homogeneous models ($R \propto \sqrt{t}$). This may be one of the reasons that explain the agreement between the Plesset-Zwick homogeneous model ($R = 1.96Ja\sqrt{\alpha_l t}$) and the Cooper microlayer model ($R = 1.9Ja\sqrt{\alpha_l t}$).

$$R = 2.5JaPr^{-1/2}\sqrt{\alpha_l t} \quad (16)$$

The excellent agreement between the two models in Fig. 10a may stimulate a debate about the extent of the contribution of the microlayer. To further investigate the contribution of the microlayer, the liquid volume in the microlayer was estimated in the present study using the measured contact radius as given by Eq. (17) and assuming that the microlayer is uniform with an average thickness ($\delta_0/2$), which may be a reasonable assumption for wedge shape microlayer. This volume was substituted in the analytical expression for bubble radius given by Cooper, which is a function of the microlayer volume as defined in Eq. (18).

$$V_{mL} = \pi r_{c,exp}^2 \frac{\delta_0}{2} \quad (17)$$

$$R = \left[\frac{3}{4}\frac{V_{mL} C_2 C_1^{1/2n}}{\pi\sqrt{\nu_l}\Delta T_w} \right]^{1/\left(2+\frac{1}{2n}\right)} \quad (18)$$

The bubble growth constant C_1 and the time exponent n were taken directly from the best fit equation of the experimental data up to 4 ms ($R = 0.75t^{0.44}$), $C_1 = 0.75$ and $n = 0.44$ and $C_2 = 0.8$. The bubble radius calculated using Eq. (18) was plotted in Fig. 10b (see the red symbols). As seen in the figure, the estimated radius agreed very well with the measured radius up to about 5 ms after

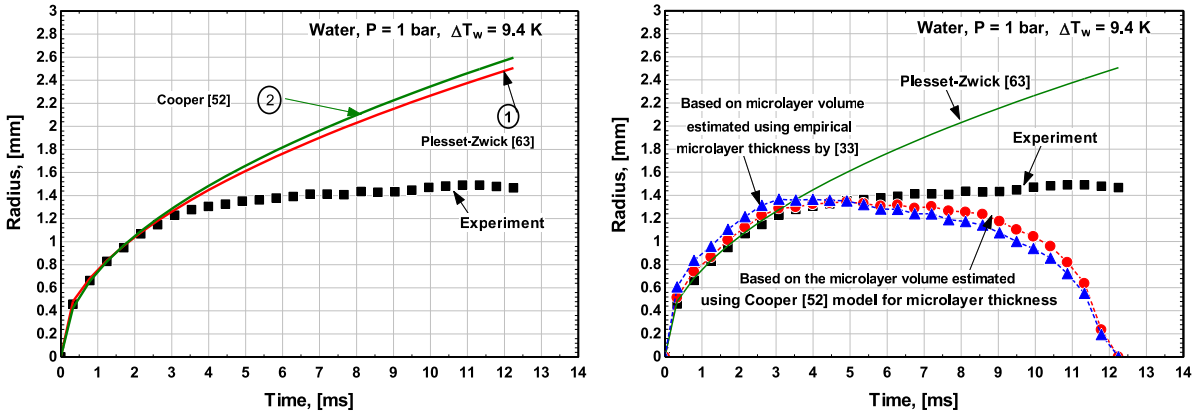

Fig. 10. Bubble radius versus time: (a) Compared with Plesset and Zwick [63] homogeneous model and Cooper [52] microlayer model, (b) Based on the experimentally determined microlayer volume using microlayer thickness given by [33] and [52].

which the radius decreased rapidly with time due to the shrinking of the contact area. The agreement of the Cooper model and experimental data verify the method of estimating the microlayer volume in the current study. The large deviation between the Cooper [52] microlayer evaporation model after 3.5 ms (in Fig. 10a) and after 5 ms (Fig. 10b) may be attributed to the fact that the model loses its physical meaning after the complete evaporation of the microlayer, which occurs when the contact radius reaches a maximum or asymptotic value. Thus, it should not be extrapolated outside its applicability range, as was used by many researchers in literature. Again, the agreement with the Plesset-Zwick homogeneous model in the first 4 ms, as seen in Fig. 10b, is not surprising because the growth constant C_1 and time exponent n were taken from the experimental power law ($R = 0.75t^{0.44}$). At this stage of discussion, it is not certain if the bubble grows due to microlayer evaporation or due to evaporation from the thermal layer around the bubble as postulated by the homogeneous model because the initial hydrodynamic microlayer thickness was dependent on the homogeneous bubble growth law. To isolate this factor, the bubble radius can be obtained directly from the estimated instantaneous liquid volume in the microlayer through a mass balance according to the following equation:

$$\rho_l V_{mL} = \rho_v V_v \text{ or } V_v = \frac{\rho_l}{\rho_v} V_{mL} \text{ or } R = \left[\frac{3V_{mL}}{4\pi}\frac{\rho_l}{\rho_v}\right]^{1/3} \tag{19}$$

The microlayer thickness needed to calculate the volume in Eq. (19) was taken this time from direct measurements (empirical) rather than a hydrodynamic model, which depends on the bubble growth law. Some researchers such as Yabuki and Nakabeppu [33] measured the local temperature and heat flux underneath the growing bubble and gave an empirical expression for the initial microlayer thickness, see Eq. (20). The radius predicted using this method (Eq. (19)) is plotted in Fig. 10b (see the blue symbols) and shows very good agreement with the experimental data as well as the hydrodynamics-based microlayer thickness suggested by Cooper [52]. Accordingly, because the radius is predicted from the liquid volume inside the microlayer, it may be concluded from this discussion that the bubble grows in the first 4 ms due to the complete evaporation of the microlayer. This is an interesting conclusion because the bubble growth can be segregated into microlayer evaporation up to about 4 ms then evaporation at the curved surface of the bubble during the rest of the growth period. Accordingly, the contribution of the microlayer evaporation to the total bubble volume may be estimated as $[100 \times (R_{e,mL}/R_d)^3]$, which gives a value of 67.8 % and the remaining 32.2 % seems to be from the curved surface of the bubble. Yabuki and Nakabeppu [33] and Tanaka et al. [45] reported 50 % microlayer contribution to bubble growth which did not vary with superheat based on local heat flux measurements using MEMS in [33] and infrared thermography in [45]. The estimated value in the present study is about 36 % larger, which may be due to the difference in thermal conductivity between copper in the present study and silicon substrate in [33] and sapphire substrate in [45].

$$\delta_0 = 4.34r^{0.69} \tag{20}$$

The above discussion proved that the bubble in Fig. (10) grows in the first 4 ms due to complete evaporation of the microlayer. Thus, the debate continues with why the homogeneous model is similar to the microlayer model? One reason may be that the bubble size in the period up to 4 ms is smaller than the thermal boundary layer thickness and thus the bubble is fully covered with the superheated layer, which is similar to homogeneous boiling. To verify this assumption, the wall thermal boundary layer and the evaporation superheat around the bubble are investigated. The evaporation superheat can be obtained from an energy balance at the bubble wall using the following equation:

$$\rho_v h_{fg}\frac{dR}{dt} = -k_l\left(\frac{\partial T}{\partial r}\right)_{r=R} = \sqrt{\frac{3}{\pi}}k_l\frac{\Delta T_w}{\sqrt{\alpha_l t}} \tag{21}$$

The bubble growth velocity required for energy balance is obtained directly from the experimental growth curve while the temperature gradient at the interface $(\frac{\partial T}{\partial r})_{r=R}$ can be obtained based on the Plesset and Zwick [63] bubble growth model. Fig. 11a depicts the predicted superheat and the measured bubble height plotted on the right vertical axis. The horizontal dashed lines indicate the edge of the wall thermal boundary layer predicted based on natural convection, i.e. $\delta_{th} = k_l/h_{nc}$, where h_{nc} is obtained from Eq (9), giving $\delta_{th} = 0.63$ mm and the actual thickness based on the measured heat transfer coefficient $\delta_{th} = k_l/h_{exp} = 0.35\ mm$, where h_{exp} is 1872 W/m^2 K. It is worth mentioning that there is no agreement on the height of the wall thermal boundary layer as discussed in the introduction section. Some researchers [41] measured thickness up to 1.3 mm and some others [38] reported smaller values. The discussion of the heat transfer mechanism presented later verified that the actual thickness, i.e. 0.35 mm, seems to be the correct thickness. Thus, this thickness is used in the current discussion. As seen in Fig. 11a, it is obvious that the height of bubbles No. 1 – 5 is larger than the actual boundary layer thickness and consequently they all protrude outside the wall thermal boundary layer. The predicted evaporation superheat for these five

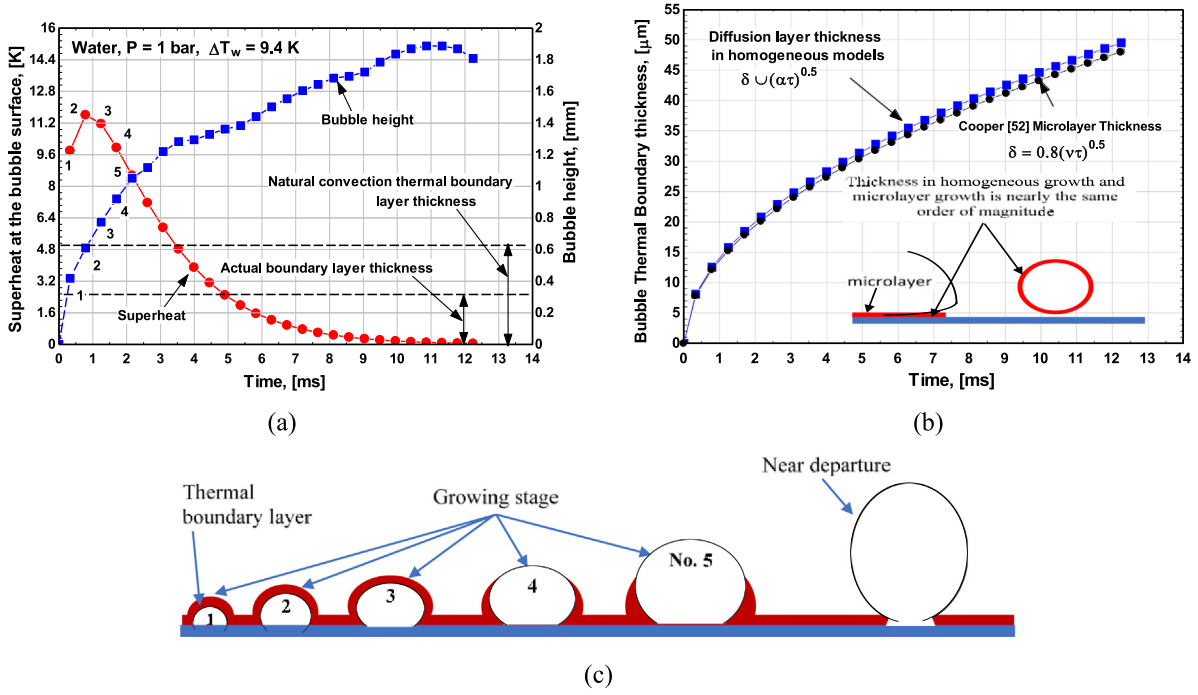

Fig. 11. Bubble growth and relation to thermal boundary layer: (a) Evaporation superheat and bubble height versus time, (b) Conduction layer thickness in homogeneous and Cooper [52] microlayer model, (c) Schematic for bubble growth in the thermal boundary layer based on (a).

bubbles (representing the early stage < 2 ms) indicated that the superheat increased to a peak value of 11.6 K at about 0.79 ms. This value is larger than the measured average superheat 9.4 K, which may indicate that the bubble is surrounded by the initial superheated layer even after it protrudes the boundary layer (see bubbles 1 – 3 in the schematic in Fig. 11c). With time, this layer was depleted due to evaporation and the superheat decreases continuously with time and part of the bubble becomes uncovered from the superheated layer as seen in bubbles 4 and 5 in the schematic. The last bubble in the schematic represents a bubble in the departure stage when the contact line shrinks and evaporation may be limited only to that part immersed in the superheated boundary layer, which could be a reason for the slow asymptotic growth stage occurring after 4 ms in Fig. 8b.

This analysis indicates that all bubbles protrude outside the thermal boundary layer and thus it could not explain why the homogeneous model agrees with the Cooper microlayer model. The possible explanation is that the microlayer is part of the total bubble interfacial area. It is worth mentioning that the heat-diffusion bubble growth in homogeneous or heterogeneous boiling is obtained from an energy balance at the interface ($q_{evp}A_{int} = q_{cond}A_{int}$). The interfacial area can be the entire surface area if the bubble is surrounded by a superheated liquid as in homogeneous boiling while it can be part of the area (microlayer) when part of the bubble is surrounded by the superheated liquid. The possible difference is the conduction layer thickness used in the two models. In homogeneous boiling, the conduction layer thickness scales with $\sqrt{\alpha_l t}$ (see Eq. (21)), while in the Cooper microlayer model it scales with $0.8\sqrt{\nu_l t}$. If the two thicknesses are the same, then the difference between the two models is expected to be small. This is very obvious from Fig. 11b which compares the conduction layer thickness in homogeneous boiling with the Cooper microlayer thickness. The insignificant difference between the thickness in the two models (about 3 %) indicates that the similarity between the two models is arising from obtaining nearly the same conduction layer thickness but using two different methods, i.e. hydrodynamic in Cooper and transient conduction in Plesset-Zwick.

3.1.4. Possible modification to homogeneous models

As discussed above, the Plesset-Zwick [63] and the Cooper [52] models are valid only during the growth period (up to about 4 ms) and the microlayer models should not be extrapolated after the complete evaporation of the microlayer. A possible modification to homogeneous models will be discussed here since homogeneous models are simple compared to most heterogeneous models. To understand why there is a large over-prediction after 4 ms, the actual available superheat can be estimated using the Plesset-Zwick [63] model by back calculations, i.e. the superheat in Jackob number was obtained by iteration until the predicted radius equals the measured bubble radius. Fig. 12a shows that the predicted superheat in the first 4 ms is nearly equal to the measured average superheat, which seems to agree with the above discussion on the superheated envelope being pushed with the bubble during this period. After 4 ms, the superheat decreased continuously with time up to departure. It is worth mentioning that there is a fundamental difference between the available superheat used in the definition of Jackob number and the effective evaporation superheat predicted in Fig. 11a. The effective evaporation superheat is driven by the velocity of the interface while the available superheat is driven by the rate of recovery of superheat from the continuous heating under the constant heat flux boundary condition. Fig. 12a indicates that the predicted available superheat after 4 ms can be fitted with Eq. (22). Because the measured average superheat is known, the intersection of the measured average superheat with the best-fit equation of the extracted superheat can give the bubble growth time, which is the time for the complete evaporation of microlayer as given by Eq. (23).

$$\Delta T_{Ja} = \frac{14.6}{t^{0.38}} [\text{in this case only : time in ms}] \tag{22}$$

$$t_{g,mL} = \left[\frac{14.6}{\Delta T_w}\right]^{1/0.38} \tag{23}$$

In conclusion, the Jackob number in homogeneous models can be defined based on the measured average superheat up to the

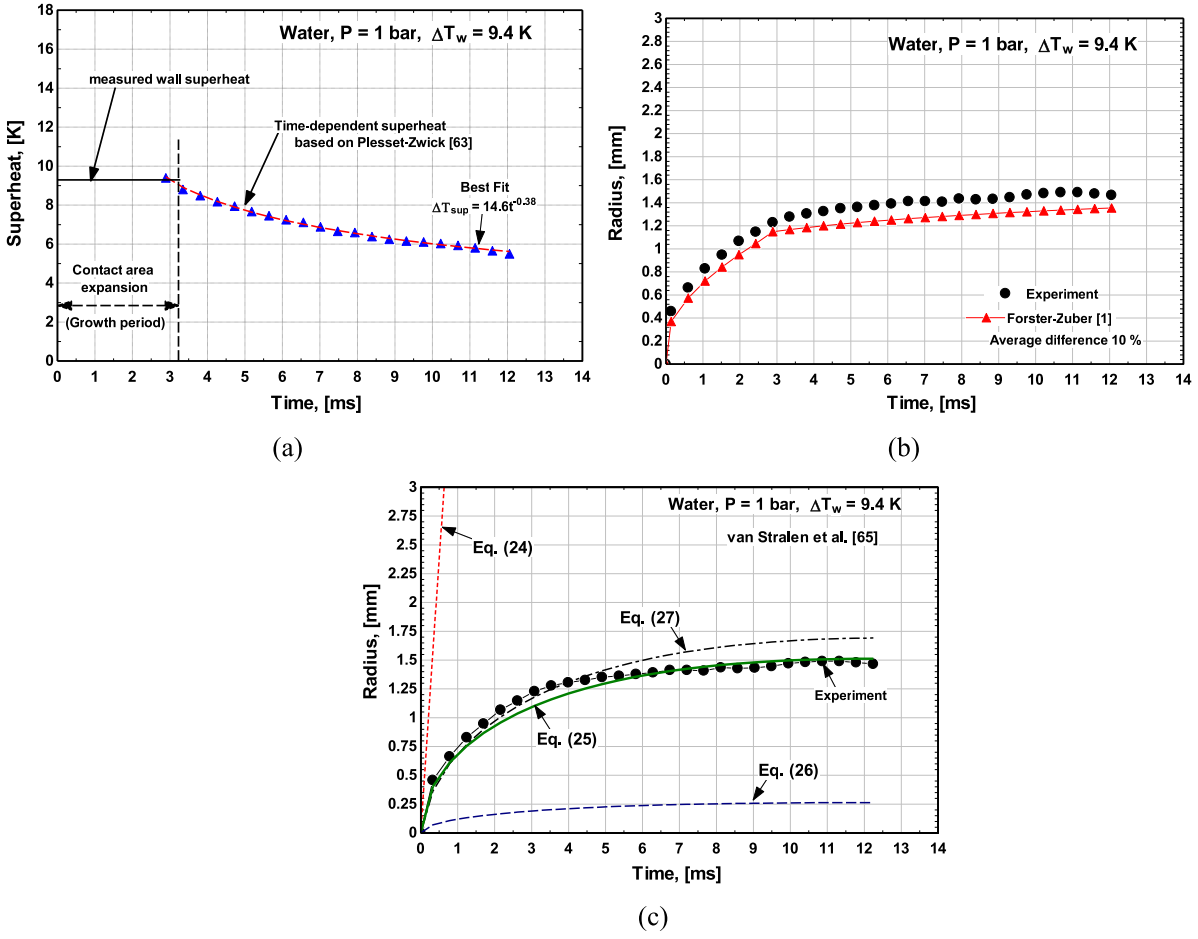

Fig. 12. Predicted degree of superheat, bubble radius with time and comparisons: (a) available superheat predicted using Plesset-Zwick model [63], (b) comparison with Forster-Zuber [1] using the time-dependent superheat, and (c) evaluation of the van Stralen et al. models [65].

time predicted from Eq. (23) then the time dependent superheat in Eq. (22) should be used in the definition of Jackob number during the rest of the growth period. This approach may be considered as a starting point in modifying the homogeneous models to be able to predict the trend of the experimental growth, which needs more experimental data. To check the validity of this approach, the fitted time-dependent superheat was used in a different model by Forster and Zuber [1] and the comparison is shown in Fig. 12b. It is obvious that the trend of the bubble growth radius using the time depended superheat can be predicted very well with an average error of 10 %. Note that using other different models may result in a curve which is shifted up or down but the trend is the same as the experimental trend. The reason of this shift is due to the curvature factor used in each model, which may need to be optimized, e.g. $\sqrt{3/\pi}$ in Plesset-Zwick [63] and $\sqrt{\pi}$ in Forster-Zuber [1]. It is worth mentioning that the time-dependent Jackob number was recommended by van Stralen et al. [65]. They gave a model that was based on inertia mechanism Eq. (24), evaporation from the bubble curved surface only (Eq. (25)), which was called by [65] the "relaxation layer", evaporation from the microlayer only Eq. (26), and a model that combines all the three mechanisms Eq. (27). In these equations, *Ja* was based on the measured average superheat which was modified by a time dependent exponential factor. To use this model, the bubble departure time must be known in advance and the value used here was from the experimental measurements. The factor b^* was used to account for the height of the bubble immersed inside the superheated boundary layer and its value was 0.792 for hemispherical bubble and ≤ 1 for spherical bubbles.

$$R_I = 0.8165t\sqrt{\frac{\rho_v h_{fg}\Delta T_w \exp -\left(\frac{t}{t_d}\right)^{1/2}}{\rho_l T_{sat}}} \tag{24}$$

$$R_{b,relax} = 1.9544\left[\left\{b^* \exp -\left(\frac{t}{t_d}\right)^{1/2}\right\} + \frac{\Delta T_{sub}}{\Delta T_w}\right] Ja\sqrt{\alpha t} \tag{25}$$

$$R_{mL} = 0.373 Pr^{-1/6} \exp -\left(\frac{t}{t_d}\right)^{1/2} Ja\sqrt{\alpha t} \tag{26}$$

$$R_{all} = \frac{R_I\left(R_{b,relax} + R_{mL}\right)}{R_I + \left(R_{b,relax} + R_{mL}\right)} \tag{27}$$

Fig. 12c shows the comparison with this model assuming $b^* = 1$. The figure indicates that the inertia growth given by Eq. (24) and the microlayer only Eq. (26) deviates significantly from the experimental data. On the contrary, the radius predicted based on evaporation from the bubble curved surface only (Eq. (25)) exhibits excellent agreement with the experimental data. It is worth mentioning that the radius predicted using Eq. (25) is exactly the same as the Plesset-Zwick [63] model if the exponential term and the effect of sub-cooling was ignored. Assuming $b^* = 1$ means that the bubble is covered with the superheated layer during the entire growth period, which may not be correct. Thus, the agreement with the experimental data seems to be due to capturing the correct trend of the time depended superheat. The failure of the microlayer model to predict the data compared to

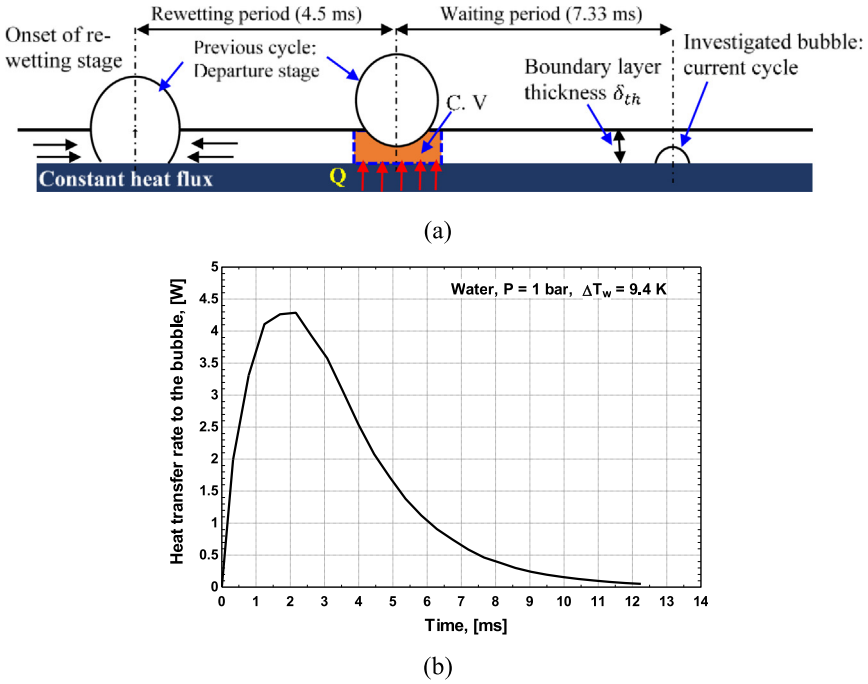

Fig. 13. Superheated layer and heat flow to the bubble: (a) schematic drawing for the recovery of the superheated layer, (b) instantaneous heat flow to the bubble during the growth period.

the Cooper model is due to the difference in the derived microlayer thickness. Additionally, because the microlayer is always at the wall, the superheat should not be time dependent as is given in Eq. (26). The bubble radius calculated using Eq. (27) that combines all three mechanisms (inertia, evaporation at bubble dome, microlayer evaporation) slightly over-predicts the data after 5 ms.

3.1.5. Heat transfer analysis

This section sheds some light on understanding the heat transfer mechanism. It may be assumed that heat is transferred from the boiling surface to the liquid first by conduction during the waiting period then from the liquid to the bubble by evaporation. If this assumption is correct, the heat taken by the bubble should be nearly equal to the sensible heat stored in the boundary layer during the waiting period. Fig. 13a depicts a schematic drawing showing the bubble under discussion (current bubble) and a bubble in the departure stage from the previous cycle to help clarify this point. The estimation of the maximum quantity of sensible heat stored in the thermal boundary layer before the appearance of the investigated bubble should be done based on the previous cycle. This is because part of the recovery of the superheated layer occurs during the rewetting stage (there is an overlapping among the cycles). An energy balance was applied to the control volume shown in the schematic of Fig. 13a and described by Eq. (28) assuming that the diameter of the area affected by the bubble equals the departure diameter (2.5 mm in the previous cycle). As seen in the schematic, the superheat recovery time should be the summation of the waiting period and the rewetting period (7.33 + 4.5 ms). It is worth mentioning that it is common in literature to assume that the recovery of the superheated layer occurs during the waiting period only. But in many cases, the waiting period is zero which may verify the overlapping assumption adopted in the current discussion. The wall thermal boundary layer thickness required for the heat balance in Eq. (28) was the actual thickness based on the measured heat transfer coefficient ($\delta_{th} = k_l/h_{exp}$ =0.35 mm).

$$Q_{sH} \times dt_{recov} = m_l c_{pl} \Delta T_w = \rho_l c_{pl} \pi R_d^2 \delta_{th} \Delta T_w \tag{28}$$

Using the above equation, the total sensible heat stored in the boundary layer during the assumed recovery period was found to be 5.52 W. This quantity of heat was based on the assumption that all the supplied heat in the rewetting stage was stored as sensible heat. However, part of this heat may be consumed in the evaporation during the rewetting period of the previous cycle (the slow growth stage). This quantity of heat was evaluated from the total heat transfer rate to the growing bubble in the previous cycle and the value was found to be 0.78 W. Thus, the net quantity of heat supplied to the bubble was (5.52 W – 0.78 W = 4.74 W). To compare this quantity of heat with the heat taken by the bubble, the instantaneous heat flow to the bubble was calculated directly from the measured growth curve using the following equation:

$$Q_{ev}(t) = \rho_v h_{fg} 4\pi R^2 \frac{dR}{dt} \tag{29}$$

The estimated instantaneous heat flow is plotted in Fig. 13b which shows that the heat transfer rate to the bubble reaches a maximum value of 4.29 W at about 2.16 ms then it decreases rapidly with time. If this maximum heat transfer rate was divided by the projected area of the bubble, the maximum local heat flux will be 3.02 MW/m^2. This value is comparable with the value reported by Tanaka et al. [45] based on infrared thermography if one considers the difference in superheat. They reported a maximum instantaneous heat flux of 4.2 MW/m^2 at 16.5 K (higher than the superheat in the current discussion, 9.4 K). When the time averaged heat flow was calculated using Eq. (30), the value was found to be 1.6 W. This means that the total latent heat taken by the bubble during the whole growth period represent only 32.7 % (1.6/4.74) of the total available sensible heat during the superheat recovery period. The remaining 67.3 % seems to be by the liquid (whether it is by transient conduction or convection or both). Based on the measured bubble growth curve and without detailed local measurements, this discussion verified that nearly most of the heat transfer from the wall is transient conduction, which agree with Ref. [49] who reported 80 %, Ref. [50] 70 %, Ref. [45] 75 % and Ref. [51] 60 – 80 %, which were based on local heat flux

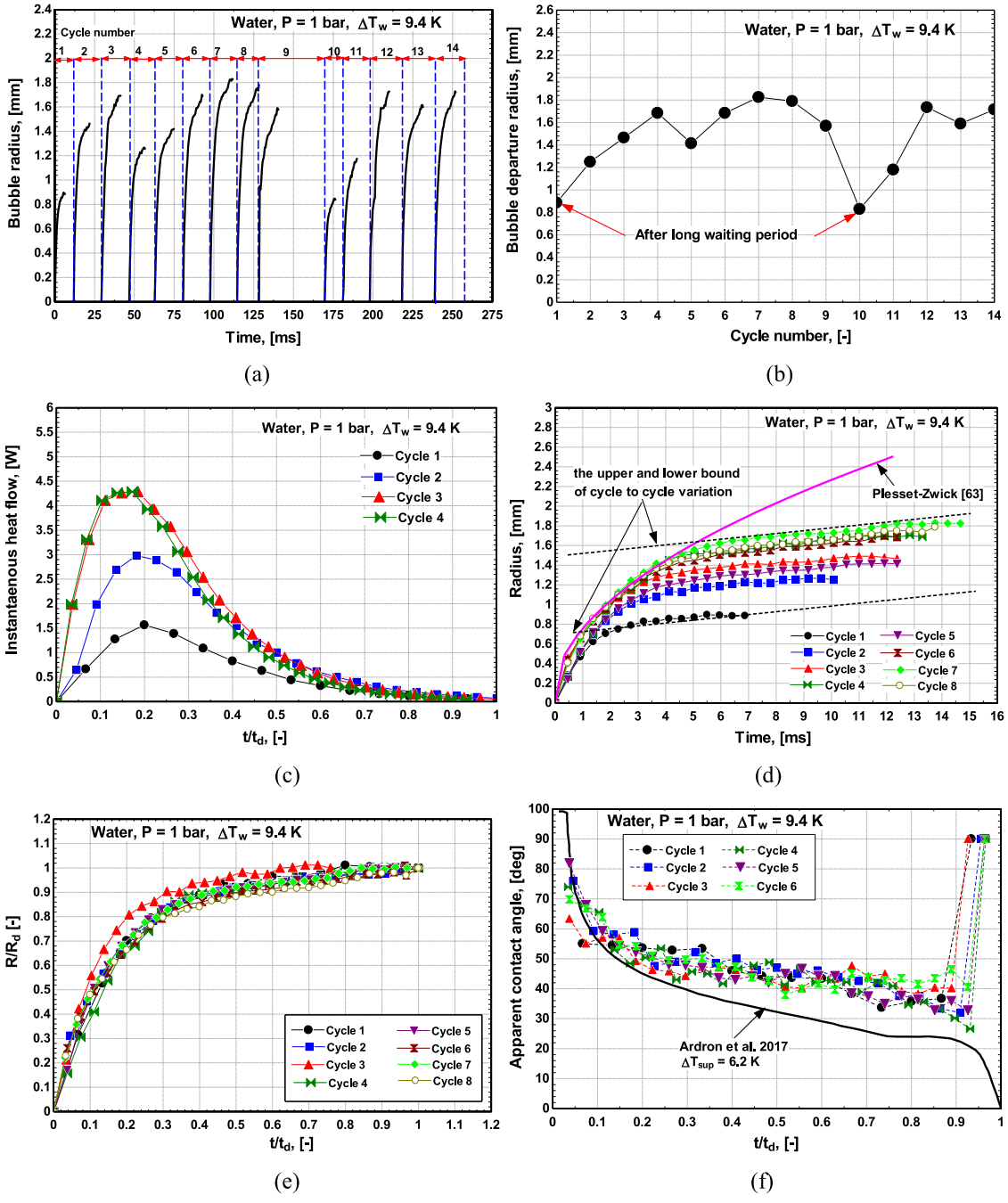

Fig. 14. Bubble growth rate from consecutive cycles and heat transfer rates: (a) bubble growth curve and (b) departure radius from 14 consecutive cycles, (c) instantaneous heat flow for 4 cycles, (d) radius versus time for 8 cycles compared with Plesset-Zwick model [63], (e) dimensionless radius versus dimensionless time, (f) apparent contact angle from 6 cycles compared to a model.

measurements.

$$Q_{av} = \frac{1}{t_d}\int_0^{t_d} Q_{ev}(t)dt \tag{30}$$

3.1.6. Bubble growth from consecutive cycles

One of the factors that may result in a discrepancy among the experimental data and the models could be the cycle to cycle variations. Fig. 14a shows the measured bubble radius versus time for 14 consecutive cycles from the same nucleation site at average superheat 9.4 K to help examine this factor. It is obvious that the bubble departure radius varies from cycle to cycle as seen in Fig. 14b. The departure radius increased in the first four cycles from 0.9 mm to 1.7 mm then it started to fluctuate up to cycle 9. After the ninth cycle, this behaviour was repeated, where the departure radius increased from 0.83 mm to 1.73 mm in the cycles 10 – 12 then starts to fluctuate. This behaviour can be attributed to variations in the waiting time. For example, the bubble in cycle 1 nucleated after a waiting period greater than 25 ms (the bubble nucleated after 25 ms from the starting point of the video). In other words, the bubble is not affected by the preceding bubble. In this case, when there is no vertical interaction, the bubble departed at smaller radius of 0.89 mm, departure time was 6.87 ms and the frequency was 84 Hz. After the first cycle, the nucleating bubble is affected by the preceding one and the departure radius increased and started to fluctuate between 1.4 and 1.8 mm

and the frequency fluctuated between 56 and 72 Hz up to cycle 8. Cycle 9 nucleated after 29 ms waiting period and thus the frequency dropped significantly to 24 Hz. It is interesting to note that after cycle 9, the bubble in cycle 10 behaved similar to the bubble in cycle 1. The departure radius was 0.83 mm and the frequency were 87 Hz compared to 0.9 mm and 84 Hz in cycle 1. Thus, based on the observed bubble shapes in these cycles, it can be concluded that the effect of the preceding bubble on the next growing bubble makes the bubble flattened with larger contact area with the surface which increases the surface tension force and evaporation from the microlayer and thus increases the bubble size compared to the first cycle when there is no vertical interaction among the bubbles. To verify that the cycle to cycle variation is due to variations in the heat flow to the bubble, the instantaneous heat flow to the bubble in the first 4 cycles (as an example) was plotted versus time normalized by the departure time as seen in Fig. 14c. As seen in the figure, the peak value in the first cycle was the smallest and increased in cycle 2 and 3 while cycle 4 was similar to cycle 3. The variation in the instantaneous heat may be attributed to variations in the initial available local superheat which seems to vary from cycle to cycle. Fig. 14d shows the difference in bubble radius versus time for eight cycles compared with the Plesset-Zwick [63] model based on the measured average superheat. Interestingly, the first growth stage (rapid growth) is not affected significantly while the difference becomes obvious in the slow growth stage. This figure reflects one of the difficulties in evaluating bubble growth models based only on one ebullition cycle. On the contrary, when the bubble radius was plotted in a dimensionless form in Fig. 14e, all curves from all cycles collapsed into one single curve. This means that bubble growth models should be presented in dimensionless form to damp the effect of local superheat. The apparent dynamic contact angle was also measured for a number of cycles as seen in Fig. 14f. The figure indicates that the bubble grows in a similar manner where the apparent contact angle exhibited the same trend. Interestingly, when the data were compared with the numerical results from Ardron et al. [66], the comparison exhibited reasonable agreement except toward departure where the model could not predict the neck. These numerical data were obtained for 6.1 K superheat which is lower than the current experiment (9.4 K). It is worth mentioning that the discussion conducted in the above sections in Figs. 7–13 was based on cycle 3 in Fig. 14a which was selected such that the effect of waiting time has diminished.

3.2. Bubble growth at sub-atmospheric pressure

3.2.1. Bubble growth curve

It is well-known that bubble size at sub-atmospheric pressure is much larger than that at atmospheric pressure. Thus, it was difficult to study bubble dynamics in the isolated bubble regime from the whole boiling surface with diameter 25 mm because bubble coalescence may spread over the whole boiling surface, especially when bubbles form at or near the edges. To overcome this issue, the entire boiling surface was masked with a polyimide tape (50 μm thick) except an active area at the middle. With this method, it was possible to generate a single bubble on the boiling surface. This can help understand the effect of superheat, which was not possible at atmospheric pressure because the nucleation site was not the same for each studied superheat. Additionally, this may quantify the latent heat contribution to the total heat transfer rate as will be discussed later in this section. Fig. 15 depicts the image sequence for one ebullition cycle at P = 0.14 bar, heat flux 16.6 kW/m^2 and superheat 15.5 K. The figure depicts that bubble growth characteristics at sub-atmospheric pressure are different compared to atmospheric pressure. The bubble grows with nearly a hemispherical shape for about 10 ms, which is much longer than the atmospheric pressure case. After 10 ms, the shape changed to a flattened spheroid up to 17.6 ms after which the spheroidal shape started vertical stretching up to departure. It is worth noting that the bubble did not show a spherical shape in the intermediate stage as was the case in atmospheric pressure. After departure, a second bubble appeared immediately without a waiting period as seen in the picture at time 27.14 ms. After about 4 ms, this bubble merged with the departed bubble at time 30.95 ms. With the progress of time, it penetrated the main bubble from the lower to the upper sides a seen in the picture at time 36.67 ms. After that the bubble exhibited a highly distorted shape from the upper side until it departed at 49.5 ms. After the departure of the two merged and distorted bubbles, the waiting period reached 39.5 ms before the appearance of a new bubble. This behaviour was repeatable and agrees with what was reported by [29,31,32], i.e. always after the departure of the main large bubble, a secondary bubble forms which destroys this bubble with a longer waiting period before the appearance of the next bubble. All bubbles discussed in this section were the bubble which appeared after the long waiting period from growth to departure, i.e. the secondary small bubble was not included.

Fig. 16a depicts the bubble radius and the contact radius plotted versus time. It demonstrates that the bubble radius increases nearly linearly with time in the beginning then the rate of growth decreased continuously as the time increased. The contact radius increased with time in the expansion stage and reached a maximum value at about 10 ms then remain unchanged for about 2 ms, which was called by [57,58] the pinning stage then it decreased rapidly with time during the contraction stage (rewetting). The contact radius was plotted in a dimensionless form R_c/R versus t/t_d in Fig. 16b for atmospheric and sub-atmospheric pressure. For sub-atmospheric pressure, the ratio was about 1 at the beginning indicating that the bubble shape was a hemisphere up to $t/t_d = 0.2$, then the ratio decreased rapidly with time indicating that the bubble shape changed to a spheroid flattened or vertically stretched. In the atmospheric pressure case, the ratio was about 0.8 at the beginning (not hemispherical) then decreased rapidly with time. The forces acting on the bubble during its growth cycle are plotted in Fig. 16c which shows that the liquid inertia force was the largest force up to 12 ms, which explains the hemispherical shape observed in this period, see Fig. 15. After 12 ms, the buoyancy force exceeded the inertia force up to the departure time. It is also obvious that the surface tension force is much smaller during the whole growth period compared to the liquid inertia and buoyancy forces, which may explain the absence of spherical bubble shape in Fig. 15 and compared to the atmospheric pressure case and may explain the dominance of the spheroidal (flattened/stretched) at sub-atmospheric pressure. Based on this figure, it may be concluded that the departure mechanism is completely different compared to the atmospheric pressure. Static force balance between surface tension and buoyancy force was sufficient to predict the departure diameter at atmospheric pressure. On the contrary, at sub-atmospheric pressure the balance should be between the liquid inertia and the buoyancy force, which can be verified using the model given by Zeng et al. [67] in Eq. (31), which was suggested based on a balance between inertia and buoyancy forces.

$$R = \left\{ \frac{3}{4} \frac{K^{2/n}}{g} \left[10n^2 + n(n-1) \right] \right\}^{n/(2-n)} \tag{31}$$

Because the buoyancy forces exceeded the inertia force after 12 ms, then the best fit equation ($R = 0.0137t^{0.29}$, t in sec and R in m) for the experimental data between 12 ms and departure should be used to predict the radius using Eq. (31). Using the growth constant (0.0137) and the time exponent 0.29 results in a bubble departure radius of 3.96 mm

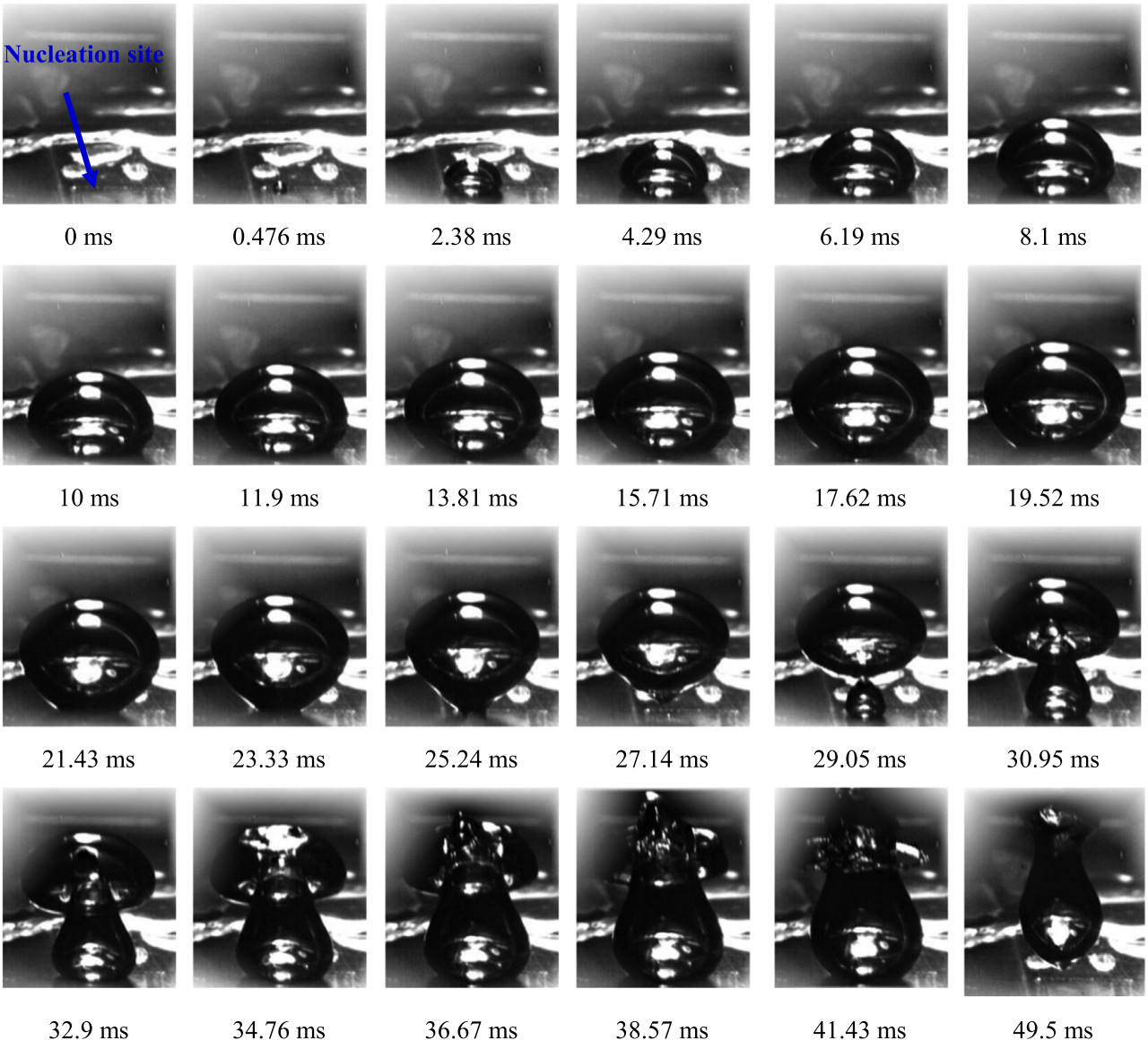

Fig. 15. Bubble growth during one ebullition cycle showing secondary bubble after the departure of the main bubble at P = 0.14 bar, q = 16.6 and $\Delta T_w = 15.5\ K$

which is 2.4 % smaller than the measured value. This calculation verifies that at sub-atmospheric pressure, bubble departure is controlled by liquid inertia and buoyancy forces. Fig. 16d shows the apparent contact angle versus time with the best fit power law which exhibited nearly a similar behaviour to the bubble discussed at atmospheric pressure. Thus, it seems that the apparent contact angle is not affected significantly by the system pressure, i.e. the apparent contact line expands and contract in a similar way.

3.2.2. Bubble growth mechanism

Similar to the discussion conducted at atmospheric pressure, to understand the bubble growth mechanism at 0.14 bar, the data were compared with the Rayleigh inertial model (Eq. (12)), the Cooper microlayer model (Eq. (16)), the Plesset and Zwick model [63] (Eq. (14)) and the Cole and Shulman [28] (Eq. (5)) models as seen in Fig. 16(a). The comparison indicates that none of the models predict the experimental data with Cole and Shulman [28] model performing better than the other models. This may be attributed to the fact that this model was an empirical model based on data at sub-atmospheric pressure. The difference with the current study may be due to differences in the experimental setup. They conducted the test on a metal strip which was directly heated and the superheat was estimated from the change in electric resistance. They reported that the uncertainty in the measured superheat was about 50 %. This means that this correlation may be affected by this large error in the measured superheat. As mentioned above, the bubble shape was hemispherical for a long period and the contact area was larger compared to the atmospheric pressure as seen in Fig. 16(b). Thus, it is expected that the contribution from the microlayer evaporation is larger than that at atmospheric pressure. However, although the Cooper [52] model was based on microlayer evaporation and developed based on sub-atmospheric data, it exhibited large deviations. The bubble growth mechanism needs to be clarified first in order to understand the reasons of the large deviation between the models and the experimental data. The growth curve in Fig. 16(a) was segregated into four segments in Fig. 17a and each segment was fitted with a power law. The first segment consists of five data points in the first 3 ms and, as can be seen in the figure, the experimental data fitted a power law with time exponent nearly 1 which supports that bubble growth in this stage is inertia-controlled. However, it did not agree with the radius predicted using the inertia-controlled

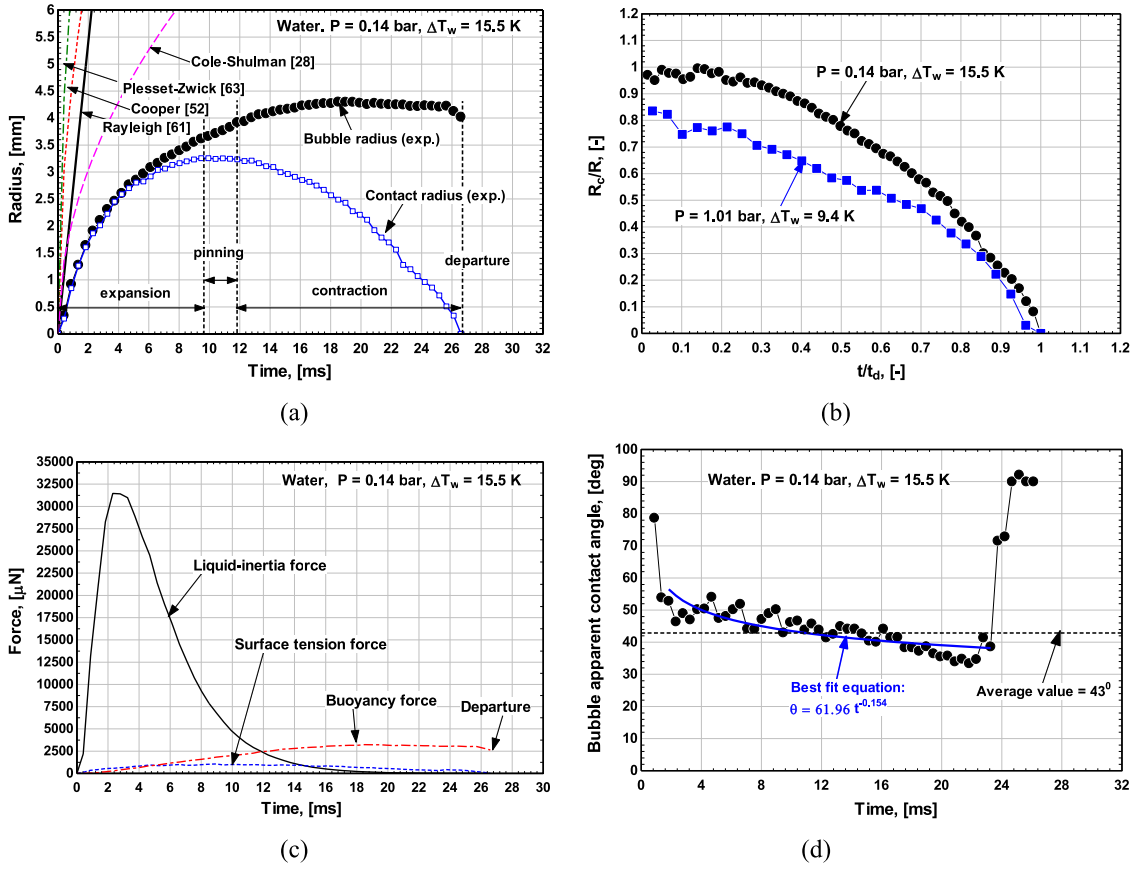

Fig. 16. Bubble growth and relevant forces at sub-atmospheric pressure: (a) bubble radius and contact radius versus time, (b) dimensionless contact radius versus dimensionless time, (c) forces acting on the bubble, (d) apparent acontact angle versus time.

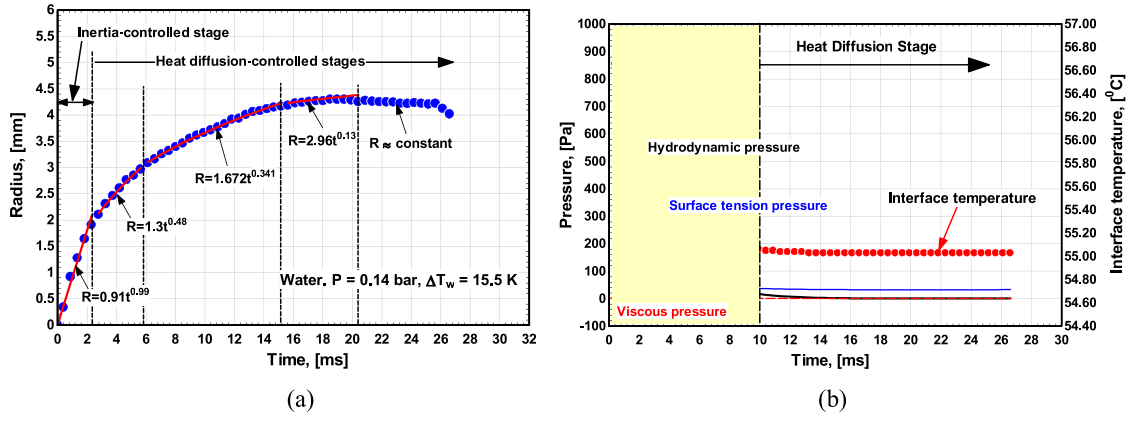

Fig. 17. Segmented and fitted bubble growth curve (a) and Hydrodynamic, surface tension and viscous pressure terms and the interface temperature versus time (b).

growth model given by the Rayleigh equation, see Fig. 16(a). This is not surprising because this equation was based on symmetrical spherical growth in homogeneous boiling, which may exhibit a larger growth constant K ($R = Kt$) because the forces acting on the bubble are only the interaction forces with the surrounding liquid and the superheat is uniformly distributed around the bubble. In nucleate boiling, the presence of the wall adds the adhesion force and makes the superheat to be non-uniformly distributed around the bubble. This may decrease the bubble growth constant compared to the homogeneous boiling. Thus, it can be concluded that the inertial-growth constant in nucleate boiling is smaller than that in homogeneous boiling, e.g. based on Fig. 17(a), $K = 0.91$ in nucleate boiling compared to $K = 2.7$ in homogeneous boiling. This conclusion may explain why the Cooper model, which was based on heat diffusion-controlled mechanism, failed to predict the experimental data. As discussed previously, this model was based on a growth law with time exponent 0.5. Investigating the second segment in the bubble growth curve which consisted of seven data points in the period 2 – 6 ms indicated that the best fit power law has a time exponent of 0.48 which is very near to the 0.5 exponent in the heat-diffusion mechanism in homogeneous boiling. The best fit power law equation in the third segment (from 6 to about 15 ms) and the fourth segment (from 15 ms to about 20 ms) exhibited a time exponent 0.34 and 0.13, respectively which are smaller than the 0.5 exponent. After the forth segment, the radius remained nearly constant and decreased slightly immediately

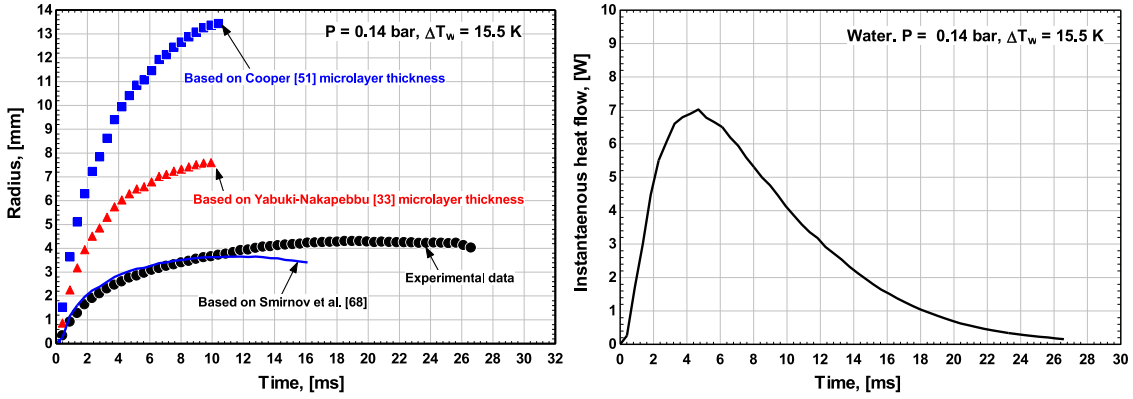

Fig. 18. Assessment of microlayer mechanism (a) and instantaneous heat flow (b).

before departure. In conclusion, based on this analysis, the inertia-controlled growth dominated up to about 3 ms while the heat diffusion growth (fast and slow) dominated the rest of the cycle. To further discuss the growth mechanism using the dynamic equation (Eq. (15)), Fig. 17(b) depicts the normal stresses at the liquid-vapour interface along with the predicted interface temperature. The figure shows that the surface tension stress diminishes very rapidly after about 2 ms, which is completely different compared to the atmospheric pressure case, see Fig. 9c. The hydrodynamic pressure (liquid inertia) diminished after about 10 ms, which corresponds to the onset of the heat diffusion-controlled mechanism. This is also obvious from the fact that the interface temperature diminishes after this time. Thus, it can be concluded based on the dynamic equation that the asymptotic growth stage (heat diffusion) dominates the growth cycle after 10 ms. At time below 10 ms, the growth is controlled by surface tension and hydrodynamic pressure in the first 2 ms, then by liquid inertia alone up to 10 ms.

3.2.3. Microlayer contribution and heat transfer analysis

The models of Cooper [52] and the Yabuki and Nakapebbu [33] for the initial microlayer thickness that were validated at atmospheric pressure are used in this section to examine their validity at sub-atmospheric pressure. The thickness predicted from these models was used to estimate the liquid volume trapped in the microlayer underneath the bubble and the bubble radius was calculated using Eq. (19) to help analyse the contribution of microlayer evaporation mechanism to bubble growth. The radius predicted using this method was plotted in Fig. 18(a) up to the end of the microlayer evaporation (maximum contact radius). As seen in the figure, the radius predicted using the microlayer thickness given by Cooper is significantly larger than the experimental data while the radius predicted using the empirical thickness given by Yabuki-Nakabeppu was in between the experimental data and the Cooper radius. This performance is expected because this empirical correlation was based on data at atmospheric pressure while the Cooper model was based on a power law of time exponent 0.5. It is well-known that the initial microlayer thickness derived from the hydrodynamic theory depends strongly on the velocity of the bubble front. The higher the velocity, the smaller the liquid film thickness. Thus, the microlayer thickness which was based on atmospheric pressure and/or low growth velocity (in the Cooper model) is expected to be much larger than that at sub-atmospheric pressure (overestimate the microlayer volume and thus larger radius). This may explain why the two models significantly overpredict the measured radius at sub-atmospheric pressure. To further examine this issue, a more general expression for the prediction of the hydrodynamic microlayer thickness was used. Smirnov et al. [68] derived a general expression (Eq. (32)) for the initial microlayer thickness which depends on the pressure difference across the interface.

$$\delta_0 = \sqrt{\frac{2\nu_l (dR/dt)}{-\frac{2}{\rho_l}\frac{dP}{dR} - \frac{d^2R}{dt^2} + \frac{2}{3}\frac{(dR/dt)^2}{R}}} \tag{32}$$

The pressure difference in the above equation was obtained directly from the dynamic equation (Eq. (15)) and the bubble growth velocity and acceleration were obtained from the experimental measurements in the early stage of growth. Thus, the initial microlayer thickness was calculated using the best fit equation in the initial growth stage (first 3 ms) which fitted a linear relation with time $R = 0.91t^{0.99}$. Assuming the microlayer has a wedge shape, the average thickness ($\delta_0/2$) was used to calculate the liquid volume trapped inside the microlayer and the radius was calculated using Eq. (19). Interestingly, the comparison exhibited excellent agreement with the experimental data up to the end of the microlayer evaporation (about 10 ms) indicating that the bubble grows due to microlayer evaporation during this period. Thus, it can be concluded that the Smirnov et al. hydrodynamic model is accurate provided that the actual experimental bubble growth equation was used to obtain the initial microlayer thickness. Additionally, the initial microlayer thickness is affected by the growth curve in the early stage rather than the growth curve along the whole growth period. Using the same assumption as atmospheric pressure, which was reported by many researchers, the microlayer evaporates completely when the contact radius reaches its maximum value. Thus, the bubble radius at the maximum contact radius can be used to estimate the contribution of the microlayer to the total bubble volume. Based on that the radius of the bubble at the end of microlayer evaporation (at maximum contact radius) was found to be 3.72 mm which is 92.5 % of the departure radius (4.02 mm). This gives a contribution of 79.2 % to the bubble volume which is somewhat larger than that at atmospheric pressure (67.8 %).

In this experiment at sub-atmospheric pressure, it is possible to examine the contribution of the latent heat transport mechanism to the total heat transfer rate since only one single bubble was generated. The analysis that was conducted at atmospheric pressure is not suitable here due to the presence of a secondary bubble after the departure of the main bubble which was not the case at atmospheric pressure. The secondary bubble made it difficult to estimate the sensible heat during the waiting period. The instantaneous heat flow to the bubble is plotted in in Fig. 18(b) which indicates that the instantaneous power reaches a maximum value of about 7 W at 5 ms then decreases rapidly with time. This

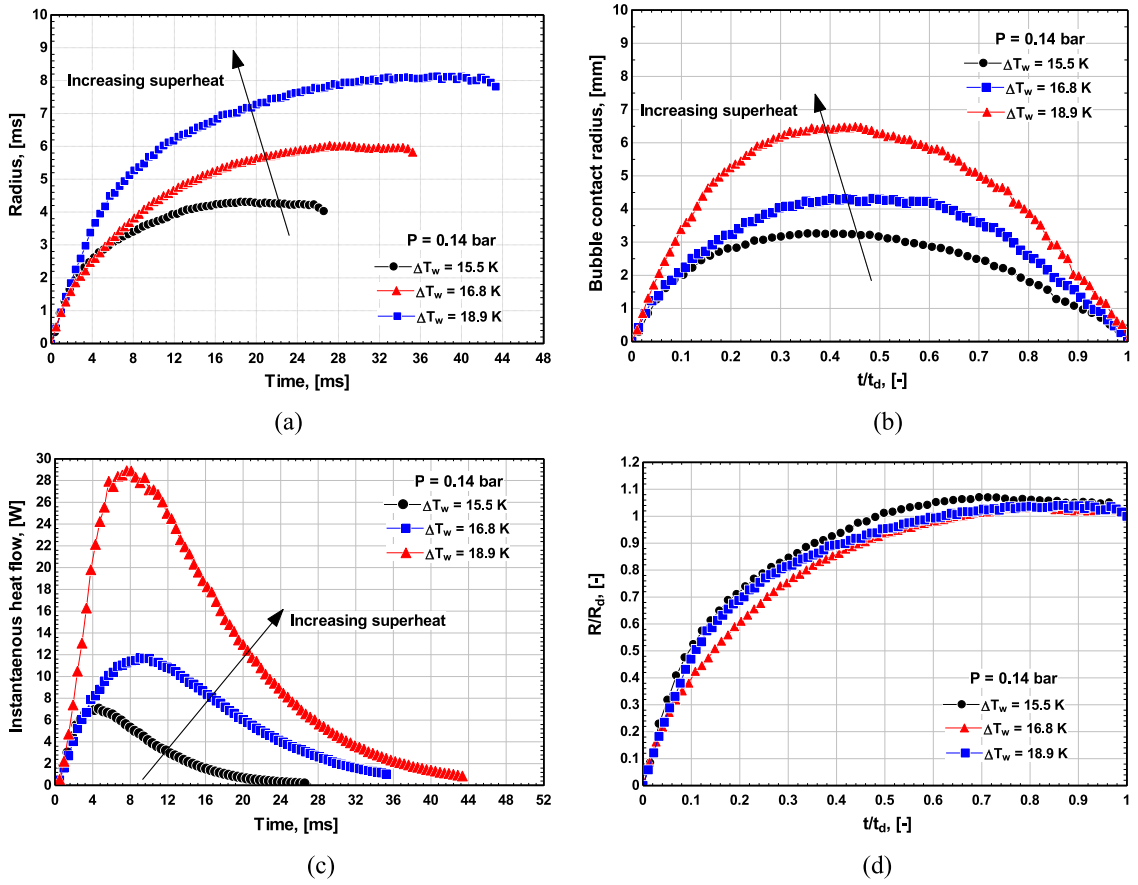

Fig. 19. Effect of superheat on (a) bubble growth curve, (b) bubble contact radius, (c) instantaneous heat rate, (d) dimensionless radius.

gives a maximum heat flux of about 0.14 MW/m^2 based on the projected area of the bubble at departure. This value is significantly smaller than the atmospheric pressure value reported in the above sections which is about 3 MW/m^2. The integration of the instantaneous curve over the departure period can give the total average heat transfer rate taken by the bubble as latent heat and calculated using Eq. (30). On doing so, the time-averaged heat transfer rate taken by the bubble as latent heat is 2.8 W. If this value was compared with the total applied power (8.15 W) based on the measured average base heat flux (16.6 kW/m^2) and the base area of the copper block (25 mm diameter), the total contribution of latent heat will be 34.4 %. The remaining 65.6 % seems to be arising from the other mechanisms present, i.e. convection and conduction.

Finally, it is important to study the effect of superheat on bubble growth in the isolated bubble regime. As previously mentioned it was difficult to capture the effect of superheat at atmospheric pressure from random cavities due to the difficulty of tracking the same nucleation site at different superheats. At sub-atmospheric pressure, the presence of one single bubble from the same nucleation site made it possible to understand the effect of superheat on bubble growth as seen in Fig. 19(a). It is obvious from the figure that the bubble growth rate, the departure radius and departure time increase as the superheat increases. Additionally, Fig. 19(b) demonstrates that the larger the superheat, the larger the apparent bubble contact radius. The increased growth rate may be attributed to the increased instantaneous heat flow to the bubble with increasing superheat as seen in Fig. 19(c). Based on the aforementioned discussion of the forces acting on the bubble, it is understood that the higher the bubble growth rate, the larger the liquid inertia force (negative force pushing the bubble towards the surface). Thus, the increase in departure radius and time may be attributed to the increase in liquid inertia force with increasing superheat. Similar to the dimensionless plot from several ebullition cycles at atmospheric pressure, Fig. 19(d) depicts the dimensionless radius versus dimensionless time as a function of superheat. The figure shows that the effect of superheat diminishes when the data are plotted in a dimensionless form. This again indicates that bubble growth data should be presented and modelled in a dimensionless form to capture the effect of variations in the local superheat.

Fig. 20(a) shows the bubble growth curve from three consecutive cycles. Because the waiting and departure time was much longer compared to atmospheric pressure case, it was not possible to track a larger number of cycles. Although the waiting time between each cycle was nearly the same and it was long enough to recover the superheated boundary layer, there is an obvious variation from cycle to cycle. In other words, there are other possible reasons for this variation, i.e. hydrodynamic effects induced by the large rising bubble or condensation effects, where the bubbles were observed to condense while rising after departure. Fig. 20(b) compares the bubble growth curve with the prediction using van Stralen et al. [65] based on evaporation from the bubble curved surface (relaxation layer) only (Eq. (25)) and microlayer only (Eq. (26)). The figure indicates that the microlayer model significantly underpredicts the experimental data while the model based on evaporation from the bubble curved surface predicts the data very well but after adjusting the empirical factor b^* to 0.042 (very small part of the bubble is inside the boundary layer). This agrees with the fact that bubble size at sub-atmospheric pressure is much larger than the wall thermal boundary layer during the entire growth period. Additionally, because this model is a ver-

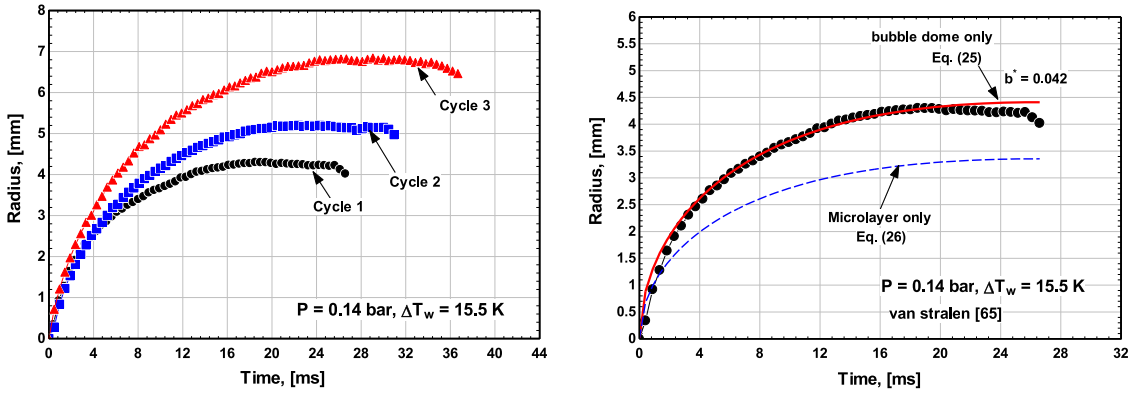

Fig. 20. Cycle to cycle variation at sub-atmospheric pressure (a) and comparison with van Stralen et al. [65] model (b).

sion of the Plesset-Zwick [6] model modified by the factor b^*, it confirms the previous discussion at atmospheric pressure for the similarity between microlayer models and homogeneous models. At atmospheric pressure the value of b^*that fitted the experimental data was 1 (the bubble remained covered with the superheated layer).

4. Conclusions

An experimental study was conducted to investigate bubble growth on a smooth thick copper surface, which is different compared to the past studies which were testing either thin or transparent surfaces. The measurements were conducted using a high-speed, high resolution camera. Although there are no detailed local heat flux measurements, the analysis of the bubble growth curve alone gave nearly qualitative and quantitative conclusions similar to studies with integrated sensors or infrared thermography. The present results constitute a good example of fundamental analysis that is possible on real engineering surfaces, using carefully calibrated temperature and flow visualisation measurements. The following conclusions can be drawn:

1 There is no big difference between the methods of estimating the bubble diameter from the captured images (i.e. using the average diameter, area-equivalent or volume-equivalent).
2 There are large variations from cycle to cycle of the bubble growth rates, the estimated heat flow and the bubble departure diameter. The reasons for this variation are difficult to determine without local measurements for the temperature and flow field.
3 Bubble growth at atmospheric pressure is divided into two stages: Rapid growth during the evaporation of the microlayer in the first few milliseconds (4 ms in our case) which is the point when the bubble contact radius reaches its maximum value; This is followed by a slower growth stage, during which heat is transferred, again by diffusion, at the lower part of the bubble still immersed in the thermal boundary layer. At sub-atmospheric pressure, bubble growth is controlled by liquid inertia in the first stage for the first few milliseconds (rapid growth, up to 3 ms in our case) followed by the slower heat diffusion stage.
4 The similarity between the Cooper microlayer evaporation model and homogeneous models at atmospheric pressure is due to similarity or small differences in the conduction layer thickness around the bubble in homogeneous boiling and the microlayer in heterogeneous boiling.
5 The data for the growth of the bubble radius versus time collapse to a single line if both the dimensionless radius (R/R_d) and time (t/t_d) are used. Similarly, it can be said that bubble growth data should be presented in a dimensionless form to capture the local variations in superheat. Additionally, the superheat should be modelled to be a time dependent. This was verified using the model by van Stralen et al. [64].

This information and conclusion in point 5 above are useful and essential when comparing and developing bubble growth models.

1 The initial microlayer thickness predicted using hydrodynamic-based models should be calculated based on the initial part of the growth curve, i.e. before the initial slope starts to change, especially when there is change in slope during the growth period. This applies to both atmospheric and sub-atmospheric pressures.
2 Microlayer evaporation contributes by about 70 % to the bubble growth regardless of system pressure. However, more than 70 % of the heat was transferred from the surface to the liquid by the mechanisms of conduction and convection. This again, is equally true for both atmospheric and sub-atmospheric pressures.
3 Bubble departure mechanism at atmospheric pressure is a balance between surface tension and buoyancy forces, while the mechanism at sub-atmospheric is a balance between buoyancy and inertia forces. At atmospheric pressure, the bubble contact radius required for surface tension force equal about 3/7 x R, i.e. the balance is not at the bubble departure moment as was recommended in the past studies.

Finally, it is worth noting that more experimental research with different fluids is needed especially with artificial cavities to capture the effect of superheat properly for the same nucleation site and correlate and validate the existing theories.

Author statement

T. G. Karayiannis planned the project. M. M. Mahmoud designed and constructed the original experimental facility under the supervision of T.G. Karayiannis. M. M. Mahmoud carried out the experiments and presented the results and first draft for changes and additions to T.G. Karayiannis. Both authors discussed the results and contributed to the final manuscript.

Declaration of Competing Interest

The authors declare that they have no known competing financial interests or personal relationships that could have appeared to influence the work reported in this paper.

Data availability

Data will be made available on request.

Acknowledgement

The work was carried out with the support of the Engineering and Physical Sciences Research Council of the UK, under Grant: EP/S019502/1.

References

[1] H.K. Forster, N. Zuber, Dynamics of vapor bubbles and boiling heat transfer, AIChE J. 1 (4) (1955) 531–535.
[2] M.M. Mahmoud, T.G. Karayiannis, Pool boiling review – Part I: fundamentals of boiling and relation to surface design, Ther. Sci. Eng. Pro. 25 (2021).
[3] D.A. Labuntsov, Approximate theory of heat transfer at advanced nucleate boiling, Izv. AN SSSR, Energetika I Transp. 1 (1963) 58–71.
[4] Y-Y. Li, Y-J. Chen, Z-H. Liu, A uniform correlation for predicting pool boiling heat transfer on plane surface with surface characteristics effect, Int. J. Heat Mass Transfer 77 (2014) 809–817.
[5] W.M. Rohsenow, A method of correlating heat transfer data for surface boiling of liquids, Trans. ASME 74 (1952) 969–976.
[6] K. Stephan, M. Abdelsalam, Heat-transfer correlations for natural convection boiling, Int. J. Heat Mass Transfer 23 (1980) 73–87.
[7] K. Nishikawa, K. Yamagata, On the correlation of nucleate boiling heat transfer, Int. J. Heat Mass Transfer 1 (1960) 219–235.
[8] B.B. Mikic, W.M. Rohsenow, A new correlation of pool-boiling data including the effect of heating surface characteristics, Trans. ASME J. Heat Transfer (1969) 245–250 May.
[9] R.J. Benjamin, A.R. Balakrishnan, Nucleate pool boiling heat transfer of pure liquids at low to moderate heat fluxes, Int. J. Heat Mass Transfer 39 (12) (1996) 2495–2509.
[10] N. Zuber, Nucleate boiling: the region of isolated bubbles and the similarities with natural conviction, Int. J. Heat Mass Transfer 6 (1963) 53–78.
[11] M. Jakob, Heat Transfer (1949) vol. 1.
[12] D.A. Labuntsov, Problems of heat transfer at nucleate boiling, Thermal Eng. 19 (9) (1972) 21–28.
[13] T. Hara, The mechanism of nucleate boiling heat transfer, Int. J. Heat Mass Transfer 6 (1963) 959–969.
[14] I.L. Mostinski, Application of the rule of corresponding states for calculation of heat transfer and critical heat flux, Teploenergetika 66 (4) (1963).
[15] D. Gorenflo, D.B.R. Kenning, H2 Pool boiling, VDI Heat Atlas, Springler-Verlag, 2009.
[16] K. Forster, R. Greif, Heat Transfer to a Boiling Liquid: Mechanism and Correlations, Progress Report no. 7(58-40) (1958) November 7.
[17] S.I. Haider, R.L. Webb, A transient micro-conviction model of nucleate boiling, Int. J. Heat Mass Transfer 40 (1997) 3675–3688.
[18] C.L. Tien, A hydrodynamic model for nucleate boiling heat transfer, Int. J. Heat Mass Transfer 5 (1962) 533–540.
[19] Y-H. Zhao, T. Masuoka, T. Tsuruta, Unified theoretical prediction of fully developed nucleate boiling and critical heat flux based on a dynamic microlayer model, Int. J. Heat Mass Transfer 45 (2002) 3189–3197.
[20] M. Kim, S.J. Kim, A mechanistic model for nucleate pool boiling including the effect of bubble coalescence on area fractions, Int. J. Heat Mass Transfer 163 (2020) 120453.
[21] V.V. Yagov, Heat transfer with developed nucleate boiling of liquids, Therm. Eng. 35 (1988) 65–70.
[22] G.N. Kruzhilin, Free conviction transfer of heat from a horizontal plate and boiling liquid, Dokl. AN SSSR (Rep. USSR Academy of Sci.) 58 (1947) 1657–1660 (In Russian).
[23] M.G. Cooper, Saturation nucleate pool boiling: a simple correlation, IChemE Symp. Ser. 86 (1984) 786–793.
[24] L.H. Chai, X.F. Peng, B.X. Wang, Nonlinear aspects of boiling systems and a new method for predicting the pool nucleate boiling heat transfer, Int. J. Heat Mass Transfer 43 (2000) 75–84.
[25] H.J. Chung, H.C. No, A nucleate boiling limitation model for the prediction of pool boiling CHF, Int. J. Heat Mass Transfer 50 (2007) 2944–2951.
[26] H. Chu, B. Yu, A new comprehensive model for nucleate pool boiling heat transfer of pure liquid at low to high heat fluxes including CHF, Int. J. Heat Mass Transfer 52 (2009) 4203–4210.
[27] B. Yu, P. Cheng, A fractal model for nucleate pool boiling heat transfer, *J. Heat Transfer* Trans. ASME 124 (2002) 1117–1124 December.
[28] R. Cole, H.I. Shulman, Bubble growth rates at high Jakob numbers, Int. J. Heat Mass Transfer 9 (1966) 1377–1390.
[29] M. Akiyama, F. Tachibana, N. Ogawa, Effect of pressure on bubble growth in pool boiling, Jpn. Soc. Mech. Engrs-Bul. 12 (53) (1969) 1121–1128.
[30] J.K. Stewart, R. Cole, Bubble growth rates during nucleate boiling at high Jakob numbers, Int. J. Heat Mass Transfer 15 (1972) 655–663.
[31] S.J.D. van Stralen, R. Cole, W.M. Sluyter, M.S. Sohal, Bubble growth rates in nucleate boiling of water at sub-atmospheric pressures, Int. J. Heat Mass Transfer 18 (1975) 655–669.
[32] W. Gao, J. Qi, X. Yang, J. Zhang, D. Wu, Experimental investigation on bubble departure in pool boiling under sub-atmospheric pressure, Int. J. Heat Mass Transfer 134 (2019) 933–947.
[33] T. Yabuki, O. Nakabeppu, Heat transfer mechanisms in isolated bubble boiling of water observed with MEMS sensor, Int. J. Heat Mass Transfer 76 (2014) 286–297.
[34] S. Jung, H. Kim, An experimental method to simultaneously measure the dynamics and heat transfer associated with a single bubble during nucleate boiling on a horizontal surface, Int. J. Heat Mass Transfer 73 (2014) 365–375.
[35] A. Surtaev, V. Serdyukov, J. Zhou, A. Pavlenko, V. Tumanov, An experimental study of vapor bubbles dynamics at water and ethanol pool boiling at low and high heat fluxes, Int. J. Heat Mass Transfer 126 (2018) 297–311.
[36] A. Surtaev, V. Serdyukov, I. Malakhov, Effect of subatmospheric pressures on heat transfer, vapour bubbles, and dry spots evolution during water boiling, Exp. Therm. Fluid Sci. 112 (2020) 109974.
[37] C-Y. Han, P. Griffith, The mechanism of heat transfer in nucleate pool boiling–Part II the heat flux-temperature difference relation, Int. J. Heat Mass Transfer 8 (1965) 905–914.
[38] B.D. Marcus, D. Dropkin, Measured temperature profile within the superheated boundary layer above a horizontal surface in saturated nucleate pool boiling of water, Trans. ASME. J. Heat Transfer (1965) 333–340.
[39] E.N. Ganic, N.H. Afgan, An analysis of temperature fields in the bubble and its liquid environment in pool boiling of water, Int. J. Heat Mass Transfer 18 (1975) 301–309.
[40] M. Takeyama, T. Kunugi, T. Yokomine, Z. Kawara, Study on superheated liquid layer in pool boiling, Int. Heat Transfer Conf., Begell House Inc (2018) 1405–1411.
[41] S. Narayan, T. Singh, A. Srivastava, Experiments on pool boiling regimes and bubble departure characteristics of single vapour bubble under subcooled bulk conditions, Exp. Therm. Fluid Sci. 111 (2020) 109943.
[42] I. Golobič, J. Petkovsek, M. Baselj, A. Papez, D.B.R. Kenning, Experimental determination of temperature wall temperature distributions close to growing vapour bubble, Heat Mass Transfer 45 (2009) 857–866.
[43] M. Zupančič, P. Zakšek, I. Golobič, Experimental investigation of single-bubble growth during the saturated pool boiling of water and self-rewetting aqueous n-butanol mixtures, Case Stud. Thermal Eng. 28 (2021) 101513.
[44] D.M. Fontana, Simultaneous measurement of bubble growth rate and thermal flux from the heating wall to the boiling fluid near the nucleation site, Int. J. Heat Mass Transfer 15 (1972) 707–720.
[45] T. Tanaka, K. Miyazaki, T. Yabuki, Observation of heat transfer mechanisms in saturated pool boiling of water by high-speed infrared thermometry, Int. J. Heat Mass Transfer 170 (2021) 121006.
[46] Y. Utaka, Y. Kashiwabara, M. Ozaki, Z. Chen, Heat transfer characteristics based on microlayer structure in nucleate pool boiling for water and ethanol, Int. J. Heat Mass Transfer 51 (1) (2014) 222–230.
[47] K. Hu, Z. Chen, Y. Utaka, Study on characteristics of formation and evaporation of microlayer using laser interferometry during nucleate pool boiling for water and ethanol, Proceeding of the of the 16th International Heat Transfer Conference IHTC-16, 2018 August 10-15.
[48] S. Narayan, A. Srivastava, On the identification and mapping of three distinct stages of single vapour bubble growth with the corresponding microlayer dynamics, Int. J. Multiphase Flow 142 (2021) 103722.
[49] M. Zupančič, P. Gregorčič, M. Bucci, C. Wang, G.M. Aguiar, M. Bucci, The wall heat flux partitioning during the pool boiling of water on thin metallic foils, Appl. Therm. Eng. 200 (2022) 117638.
[50] C. Gerardi, J. Buongiorno, L-W. Hu, T. Mckrell, Study of bubble growth in water pool boiling through synchronized infrared thermometry and high-speed video, Int. J. Heat Mass Transfer 53 (2010) 4185–4192.
[51] M. Kim, S.J. Kim, Study on the heat transfer mechanism in nucleate boiling of water by measuring local heat flux and temperature, in: Proceedings of the 17th Inter Society Conference on Thermal and Thermomechanical Phenomena in Electronic Systems, ITherm, 2018, pp. 620–629. 2018, 8419612.
[52] M.G. Cooper, The microlayer and bubble growth in nucleate pool boiling, Int. J. Heat Mass Transfer 12 (1969) 915–933.
[53] H.W. Coleman, W.G. Steele, Experimentation, Validation, and Uncertainty Analysis for Engineers, 3rd ed., John Willey and Sons Inc., NJ, USA, 2009.
[54] T.L. Bergman, A.S. Lavine, F.P. Incropera, D.P. Dwitt, Fundamentals of Heat and Mass Transfer, 7th ed., John Willey and Sons Inc., NJ, USA, 2011.
[55] S. Narayan, A. Srivastava, S. Singh, Rainbow Schlieren-based direct visualization of thermal gradients around single vapour bubble during nucleate boiling phenomena of water, Int. J. Multiphase Flow 110 (2019) 82–95.
[56] M.A. Johnson, J.R. Javier De La Peña, R.B. Mesler, Bubble shapes in nucleate boiling, AIChE J. (1966) 344–348.
[57] S.H. Kim, G.C. Lee, J.Y. Kang, K. Moriyama, H.S. Park, M.H. Kim, The role of surface energy in heterogeneous bubble growth on ideal surface, Int. J. Heat Mass Transfer 108 (2017) 1901–1909.
[58] T.P. Allred, J.A. Weibel, S.V. Garimella, The role of dynamic wetting behavior during bubble growth and departure from a solid surface, Int. J. Heat Mass Transfer 172 (2021) 121167.
[59] M. Bucci, J. Buongiorno, M. Bucci, The not-so-subtle flaws of the force balance approach to predict the departure of bubbles in boiling heat transfer, Phys. Fluids 33 (1) (2021) 017110.
[60] W. Fritz, Berechnung des maximal volume von dampf blasen, Phys. Z. 36 (1935) 379–388.
[61] Phil. Mag. XXXIV: 94, 1917 J.W.S. Rayleigh, L.S. Tong, Y.S. Tang, Boiling Heat Transfer, 2nd ed. CRL Press, 2010.

[62] B.B. Mikic, W.M. Rohsenow, P. Griffith, On bubble growth rates, Int. J. Heat Mass Transfer 13 (1970) 657–666.
[63] M.S. Plesset, S.A. Zwick, The growth of vapour bubbles in superheated liquids, J. Appl. Phys. 25 (4) (1954) 493–500.
[64] A.J. Robinson, R.L. Judd, Bubble growth in uniform and spatially distributed temperature field, Int. J. Heat Mass Transfer 44 (14) (2001) 2699–2710.
[65] S.J.D. van Stralen, M.S. Sohal, R. Cole, W.M. Sluyter, Bubble growth rates in pure and binary systems: combined effect of relaxation and evaporation microlayers, Int. J. Heat Mass Transfer 18 (1975) 453–467.
[66] K.H. Ardron, G. Giustini, S.P. Walker, Prediction of dynamic contact angles and bubble departure diameters in pool boiling using equilibrium thermodynamics, Int. J. Heat Mass Transfer 114 (2017) 1274–1294.
[67] L.Z. Zeng, J.F. Klausner, R. Mei, A unified model for the prediction of bubble detachment diameters in boiling systems – I. Pool boiling, Int. J. Heat Mass Transfer 36 (9) (1993) 2261–2270.
[68] G.F. Smirnov, Calculation of the initial thickness of the microlayer during bubble boiling, Odessa technological institute of the refrigeration Industry, Translated from In-zhenerno-Fizicheskii Zhurnal 28 (3) (1975) 503–508 March.